

HYDROGEN EMBRITTLEMENT OF THE COARSE GRAIN HEAT AFFECTED ZONE OF A QUENCHED AND TEMPERED 42CrMo4 STEEL

A. Zafra^{1*}, J. Belzunce*, C. Rodríguez*, I. Fernández-Pariente*

¹Corresponding author: Alfredo Zafra García (+34 985182023) zafraalfredo@uniovi.es

*University of Oviedo, campus universitario, east building, 33203, Gijón, Spain

ABSTRACT

The coarse grain heat affected zone (CG-HAZ) of welds produced in a quenched and tempered 42CrMo4 steel was simulated by means of a laboratory heat treatment consisting in austenitizing at 1200°C for 20 minutes, oil quenching and finally applying a post weld heat treatment at 700°C for 2 hours (similar to the tempering treatment previously applied to the base steel). A tempered martensite microstructure with a prior austenite grain size of 150 µm and a hardness of 230 HV, similar to the aforementioned CG-HAZ weld region, was produced. The effect of the prior austenite grain size on the hydrogen embrittlement (HE) behaviour of the steel was studied comparing this coarse-grained microstructure with that of the fine-grained base steel, with a prior austenite grain size of 20 µm.

The specimens used in this study were charged with hydrogen gas in a reactor at 19.5 MPa and 450°C for 21 hours. Cylindrical specimens were used to determine hydrogen uptake and hydrogen desorption behaviour. Smooth and notched tensile specimens tested under different displacement rates were also used to evaluate HE.

Embrittlement indexes, EI, were generally quite low in the case of hydrogen pre-charged tensile tests performed on smooth tensile specimens. However, very significant embrittlement indexes were obtained with notched tensile specimens. It was observed that these indexes always increase as the applied displacement rate decreases. Moreover, hydrogen embrittlement indexes also increase with increasing prior austenite grain size. In fact, the embrittlement index related to the reduction in area, EI_(RA), reached values of over 20% and 50% for the fine and coarse grain size steels, respectively, when tested under the lowest displacement rates (0.002 mm/min).

A comprehensive fractographic analysis was performed and the main operative failure micromechanisms due to the presence of internal hydrogen were determined at different test displacement rates. While microvoids coalescence (MVC) was found to be the typical ductile failure micromechanism in the absence of hydrogen in the two steels, brittle decohesion mechanisms (carbide-matrix interface decohesion, CMD, and martensitic lath interface decohesion, MLD) were observed under internal hydrogen. Intergranular fracture (IG) was also found to be operative in the case of the coarse-grained steel tested under the lowest displacement rate, in which hydrogen accumulation in the process zone ahead of the notch tip is maximal.

KEYWORDS: Hydrogen embrittlement, 42CrMo4 steel, weld heat affected zone, notched tensile strength, failure micromechanisms.

1. INTRODUCTION

Hydrogen is considered a future alternative energy source to fossil fuels. Commercial fuel cell vehicles and hydrogen refuelling stations are currently in construction in many industrialised countries. In these hydrogen infrastructures, different metallic components such as hydrogen pressure vessels, pipes and valves are directly exposed to high-pressure hydrogen gas environments of up to 70 MPa [1, 2]. The application of high-strength low-alloyed steels for these components enables lighter products in addition to weight and construction cost reductions. However, it is also now well known that high-strength steels undergo hydrogen embrittlement during their service life under high hydrogen pressure: their tensile strength and fracture toughness decrease and their fatigue crack propagation rate increases [3, 4]. The use of low- or medium-carbon, low-alloyed, quenched and tempered steels is a good choice to address these problems [5-8].

In this context, hydrogen embrittlement and the high cost of hydrogen storage vessels are important problems that hinder the development of hydrogen fuel cell vehicles and, in particular, refuelling station buffers [9, 10]. It is also worth noting that the most economical way to produce high capacity pressure vessels to contain hydrogen gas under high pressure is by means of bending and then welding heavy steel hot rolled plates using appropriate welding procedures and well-designed post-welding heat treatments (PWHT). It is well known that the applied weld thermal cycle has a significant effect on the microstructure heterogeneity of the heat affected zone and, consequently, on the susceptibility to hydrogen embrittlement [11-13]. In this respect, the mechanical properties of the base metals, heat affected zones and weld metals in different steel welded joints in the presence of hydrogen have been studied by several authors [14-17], the coarse grain heat affected zone being the region of the weld with the lowest toughness as well as the most embrittled region due to the entrance of hydrogen [11, 18, 19].

On the other hand, when evaluating the interaction between hydrogen atoms, the microstructure of the steels and the applied loads, there are two basic ways to analyse the effects of hydrogen on the mechanical properties of steels: testing in high pressure hydrogen gas (external hydrogen), and testing in air after pre-charging the specimens in a hydrogen-charged medium (internal hydrogen) [2]. In the case of external hydrogen provided by high hydrogen pressures, the measurement of mechanical properties requires the use of very expensive, unique facilities, as material test specimens are exposed to high-pressure hydrogen gas while simultaneously being subjected to specific mechanical loads. However, specimens can be both easily and conveniently pre-charged at high temperature from a gaseous atmosphere (as hydrogen diffusion depends exponentially on temperature, the use of high temperatures greatly accelerates pre-charging and provides high hydrogen contents after relatively short charging times). On the other hand, hydrogen electrochemical charging from aqueous solutions at room temperature is not recommended to simulate hydrogen gas atmospheres, as hydrogen fugacity associated with electrolytic pre-charging can be a number of orders of magnitude greater than that obtained in hydrogen gas. Furthermore, hydrogen penetration into low-diffusivity alloys is limited, often leading to large hydrogen concentration gradients near the surface of the test specimen [20].

It is also well known that the presence of internal hydrogen modifies the failure micromechanisms operative on steels submitted to mechanical loads as a consequence of hydrogen embrittlement phenomena. Although different mechanisms of hydrogen embrittlement can take place in steels and other metallic materials, such as those based on hydride-formation, hydrogen-enhanced decohesion, hydrogen-enhanced localised plasticity, adsorption-induced dislocation emission, and hydrogen-vacancy interactions, regarding internal hydrogen embrittlement, that involves diffusion and accumulation of pre-existing hydrogen in notched regions submitted to high hydrostatic stresses, the two most relevant micromechanisms in the case of steels are hydrogen-enhanced decohesion (HEDE) and hydrogen-enhanced localised plasticity (HELP) [21]. The decohesion theory, already suggested by Troiano [22] and developed later by Oriani [23], proposes that hydrogen decreased the interatomic bonds between in adjacent crystallographic planes, grain boundaries or other internal interfaces. On the other hand, Birnbaum, Sofronis, Robertson and co-workers from 1980 onwards [24-26] proposed that, since hydrogen accumulated in the region located ahead of a crack or a notch, due to the high hydrostatic stress characteristic on these regions, deformation localises in these regions as the presence of solute hydrogen facilitates dislocation activity (hydrogen reduces the Peierls stress for dislocation movement). The former mechanism gives rise to cleavage or intergranular failures, while the latter produces shallow dimples with ductile appearance.

The main objective of this paper was thus to study hydrogen embrittlement phenomena and failure micromechanisms operative in the coarse grain heat affected zone (CG-HAZ) of a 42CrMo4 base steel. The particular weld region studied on this paper was reproduced by means of an appropriate simulative laboratory heat treatment, subsequently comparing the behaviour of both the fine-grained base steel and the coarse-grained steel under the presence of hydrogen. Tensile tests were accordingly performed on both smooth and circumferentially-notched round-bar specimens pre-charged with gaseous hydrogen and failure micromechanisms were evaluated.

2. EXPERIMENTAL PROCEDURE

2.1 Material

A 42CrMo4 steel (similar to AISI 4140), whose chemical composition in weight % is shown in Table 1, was used in the present study.

Steel	C	Cr	Mo	Mn	Si	Cu	V	P	S
42CrMo4	0.42	0.98	0.22	0.62	0.18	0.02	0.01	0.008	0.002

Table 1. Chemical composition of 42CrMo4 steel (weight %)

This is a medium-carbon, Cr-Mo alloyed steel that is frequently used in quenched and tempered condition when a good combination of strength and toughness is required [27, 28]. The 42CrMo4 steel grade was austenitized at 845°C for 45 minutes, quenched in water and tempered at 700°C for 2 hours. The microstructure, tensile properties, fracture toughness and fatigue crack propagation rate of this steel grade (denominated 42CrMo4_845-700 or fine-grained) in the presence of internal hydrogen had already been studied in previous papers [4, 27, 28, 29].

2.2 Welding procedure and HAZ characterization

Semi-automatic welding using a preheating temperature, T_p , of 200°C was employed to deposit a weld bead from a carbon steel wire onto a 12 mm thick 42CrMo4 steel plate. Table 2 shows the welding parameters used for the deposition of the weld bead. The heat input, H , was calculated according to Equation (1):

$$H = 0.8 \frac{V \cdot I}{v} \quad (1)$$

Where 0.8 is the estimated efficiency of the welding process and, V , I and v , respectively represent the voltage, current and weld speed applied.

V	I	v	H
[V]	[A]	[mm/min]	[kJ/mm]
30	200	165	1.96

Table 2. Welding parameters (semi-automatic welding), $T_p=200^\circ\text{C}$

After carefully cutting the specimen (to avoid microstructural alteration), the weld was then metallographically prepared (grounded and polished with 6 and 1 μm diamond paste) and etched with Nital 2%. Measurements of Vickers microhardness (HV_1) were carried out in the CG-HAZ, very close to the fusion line (first 200 μm), applying a load of 1000 g for 15 s. At least ten measurements were made, and the average hardness value was calculated. Finally, the microstructure of the CG-HAZ was observed using an optical microscope (Nikon Epiphot 300) and a scanning electron microscope (SEM JEOL-JSM5600) under an acceleration voltage of 20 kV. Due to the high hardness measured in the aforementioned region and in order to promote microstructural homogeneity and stress relaxation, a post welding heat treatment (tempering at 700°C for 2 h) was finally applied (the same treatment as the tempering treatment previously applied to the 42Cr4Mo base steel). Microstructural characterization and microhardness measurements (HV_1) were also performed on the PWHT CG-HAZ following the aforementioned procedure.

2.3 CG-HAZ reproduction by means of an appropriate laboratory heat treatment

The approximate cooling rate at a temperature, T , of 700°C of the heat affected zone produced on the deposition of a weld bead under a preheat temperature, T_p , of 200°C, was estimated according to Equation (2), developed by Rosenthal [30]. The thermal conductivity, λ , of the 42CrMo4 steel was taken as 31 W/mK [31].

$$v_c = 2\pi\lambda \frac{(T - T_p)^2}{H} \quad (2)$$

A cooling rate at 700°C of 25 K/s was thus obtained. This cooling rate can alternatively be obtained at the mid-thickness of a large 12 mm thick steel plate quenched in oil [32].

Additionally, it is necessary to apply a very high austenitization temperature to reproduce the coarse austenitic grain size present in the CG-HAZ, although the time at high temperature must be limited in order to avoid oxidation and decarburization phenomena. Consequently, a heat treatment consisting of austenitization at 1200°C for 20 minutes followed by oil quenching was applied to specimens measuring 250 mm x 125 mm, with a thickness of 12 mm. The steel grade thus obtained, denominated 42CrMo4_1200, was characterized by means of hardness measurements (HV_{30}) using a 30 kg load applied for 15 s (five measurements) and microstructural analysis.

Finally, similarly to the CG-HAZ of the weld, a post welding heat treatment (tempering at 700°C for 2h) was also applied to the simulated CG-HAZ sample, obtaining the steel grade denominated 42CrMo4_1200-700 or coarse-grained. Microstructural characterization and HV_{30} hardness measurements were subsequently performed on this steel.

2.4 Hydrogen embrittlement study of the reproduced CG-HAZ microstructure

2.4.1 Hydrogen charging

All the specimens used in this study were pre-charged with pure gaseous hydrogen in a high-pressure reactor (with a diameter of 73 mm and a total length of 180 mm), manufactured in accordance with the ASTM G146 standard [33]. Before hydrogen charging, air was removed from the vessel using three alternate inert gas purges to reduce the oxygen level to a minimum.

In order to ensure that all the specimens were saturated with hydrogen (the maximum thickness of the tested specimens was 10 mm), the following conditions were applied: 21 hours at 450°C under a pressure of 19.5 MPa of pure hydrogen [27-29].

The high temperature hydrogen solubility of the quenched and tempered 42CrMo4 steel grades under high pressure and high temperature hydrogen gas can be approximated by the equilibrium lattice hydrogen content of BCC iron, as reported by Hirtz [34], using Equation (3), considering that microstructural traps are not active at this high temperature:

$$C_H = 104.47 \cdot \sqrt{f} \cdot e^{(-28600/RT)} \quad (3)$$

where f represents the fugacity in MPa. According to San Marchi [35], fugacity can be expressed in terms of hydrogen pressure (p) according to Equation (4):

$$f = p \cdot e^{(bp/RT)} \quad (4)$$

where b is a constant with a value of 15.84 when the pressure (p) is expressed in MPa. Applying these equations to our hydrogen charging conditions, a hydrogen content of 4.1 ppm was thus introduced into the 42CrMo4 steel samples.

After keeping the specimens in the hydrogen reactor for 21 hours, a cooling phase of 1 hour until reaching a temperature of 85°C was always necessary before allowing them to be removed from the reactor. Although the hydrogen pressure was maintained during cooling, the decrease in temperature creates a thermodynamic driving force for hydrogen egress from the specimens, leading to a significant hydrogen loss in all cases. The hydrogen pre-charged specimens were then removed from the reactor and rapidly immersed in liquid nitrogen (-196°C), where they were kept until the moment of testing in order to avoid additional hydrogen losses.

2.4.2 Measurement of hydrogen content (desorption curves)

The hydrogen content in the specimens was measured by means of thermal desorption analysis (TDA), using a LECO DH603 hydrogen analyser. The measurement principle of the equipment is based on the difference in thermal conductivity between a reference gas flow of pure nitrogen and a secondary flow composed of nitrogen and the hydrogen thermally extracted from the analysed specimen.

The hydrogen desorption curves of the two steel grades (fine-grained and coarse-grained) were determined at room temperature. These curves represent the hydrogen content versus time elapsed at room temperature (ppm vs. time). Hydrogen pre-charged cylindrical pins with a diameter of 10 mm and a length of 30 mm (≈ 20 g) were used to obtain the RT desorption curves.

The procedure to obtain the desorption curves was the following. All the hydrogen pre-charged pins were removed from the liquid nitrogen at the same time and left in air at RT. The hydrogen concentration of the different samples was then measured at different time intervals. Before starting the measurement, each pin was cleaned in an ultrasonic bath with acetone for 5 minutes and carefully dried using cold air. The analysis to determine the hydrogen concentration consisted in keeping the sample at 1100°C for 400 s.

2.4.3 Determination of the hydrogen diffusion coefficient at room temperature

Numerical fitting of the experimentally measured hydrogen desorption data was used to estimate the apparent hydrogen diffusion coefficient (D_{app}) of both steel grades. An axisymmetric bi-dimensional diffusion analysis of the aforementioned cylindrical samples was performed using a commercial FEM software (Abaqus CAE), employing 4-node linear axisymmetric quadrilateral elements, with a size of 1 mm (see Fig. 1). The initial hydrogen content experimentally determined at the end of the cooling phase (from 450 to 85°C in the high-pressure reactor) by means of the LECO analyser was taken as the first point of the analysis (boundary condition 1, BC1). The residual hydrogen content after a long stay at room temperature (about one month), likewise determined using the LECO analyser, was taken as our surface condition (boundary condition 2, BC2), namely the deep trapped hydrogen concentration in the steel.

Fick's diffusion law, described by Equation (5), was applied to a cylinder with a radius, R , of 5 mm, J being the hydrogen flux, D_{app} the apparent diffusion coefficient, and C_H the hydrogen concentration in the specimen. Although hydrogen transport is concentration dependent and also depends on the density and energy of traps [36], a constant diffusion coefficient was used in this simple study:

$$J = -D_{app} \nabla C_H \quad (5)$$

The evolution of hydrogen over time at room temperature (only radial diffusion was considered) was calculated by varying the apparent diffusion coefficient (D_{app}). The diffusion coefficient which best fitted the experimental data was taken as the apparent diffusion coefficient of the steel.

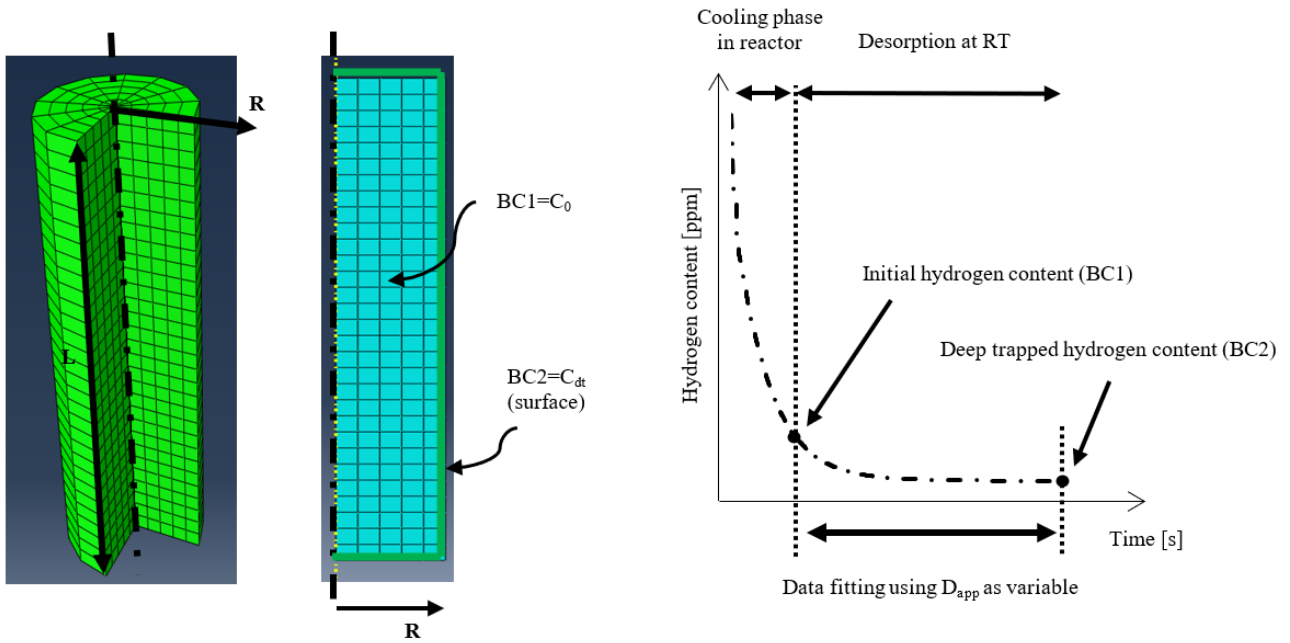


Fig. 1. Meshed sample and boundary conditions used to estimate D_{app} in radial hydrogen desorption at room temperature on hydrogen pre-charged samples (radius $R=5$ mm and length $L=30$ mm).

2.4.4 Tensile tests

Tensile tests on both smooth and circumferentially-notched round-bar specimens, whose dimensions and geometries are shown in Fig. 2, were performed in air at room temperature on an Instron 5582 tensile testing machine, following the indications given by the ISO 6892-1:2017 standard [37]. Longitudinal deformation of the specimens throughout the course of the tests was measured by means of an Instron 2630-100 extensometer with a calibrated length of 25 mm.

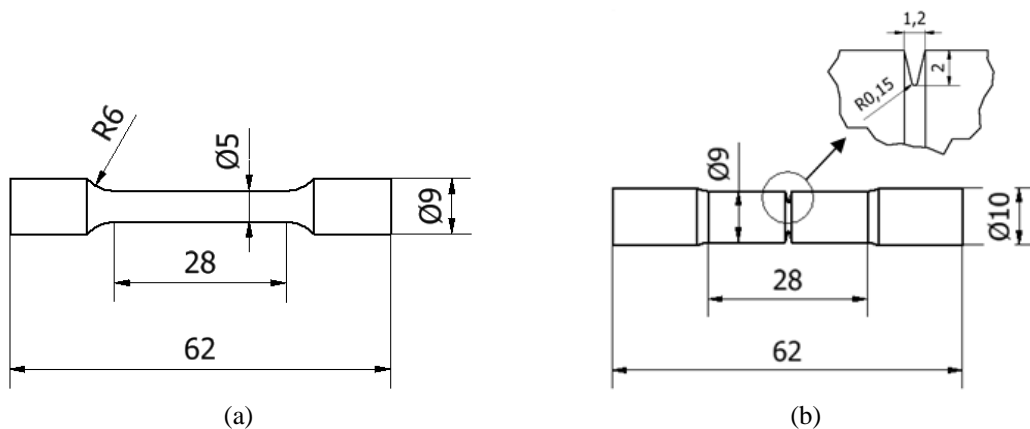


Fig. 2. Geometry and dimensions (mm) of the (a) smooth and (b) notched specimens used in the tensile tests.

The notched tensile specimens had a notch root radius of 0.15 mm and a radius of the notch cross-section of 5 mm, its corresponding stress concentration factor being $k_t = 4.3$, according to Neuber [38]. This value is in line with those calculated by other authors for similar specimen geometries [39, 40].

The behaviour of uncharged and hydrogen pre-charged specimens was compared in these tests. All the uncharged tests were performed under a displacement rate of 0.4 mm/min. However, different displacement rates, 0.4, 0.04, 0.004 and even 0.002 mm/min, were applied in the case of the hydrogen pre-charged specimens with the aim of studying the influence of this parameter on hydrogen embrittlement (HE).

In the case of the notched specimens, the engineering notched tensile strength, σ_N , was defined as the maximum tensile load divided by the initial cross-sectional area of the notch region. The extent of hydrogen embrittlement was assessed by means of the embrittlement index (EI), defined in Equation (6). EI varies from 0 (no embrittlement at all) to 100% (maximum possible hydrogen embrittlement).

$$EI [\%] = \frac{X - X_H}{X} \cdot 100 \quad (6)$$

where X and X_H are the measured steel property evaluated without and with hydrogen, respectively.

2.4.5 Observation of fracture surfaces

In order to identify the operative fracture micromechanisms, the fracture surfaces of all the tested specimens (both uncharged and hydrogen pre-charged) were analysed using a scanning electron microscope (SEM JEOL-JSM5600) under an acceleration voltage of 20 kV and different magnifications.

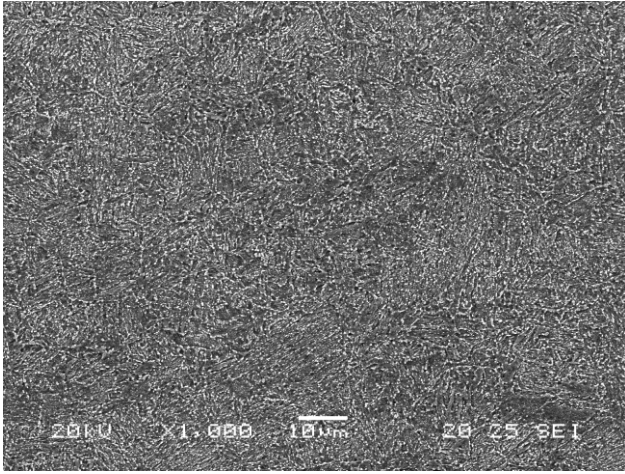
3. RESULTS

3.1 Microstructure and hardness

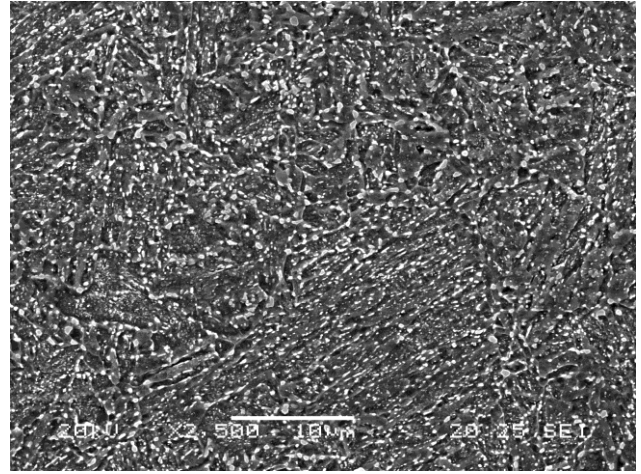
The microstructure of the original 42CrMo4 base steel, austenitized at 845°C for 45 minutes, quenched in water and tempered at 700°C for 2h (42CrMo4_845-700, fine-grained), is shown in Fig. 3 (a, b). It consists of tempered martensite, with a HV_{30} hardness of 207 and an average prior austenite grain size of 20 μm .

Fig. 3. SEM microstructures. (a, b) 42CrMo4_845-700 steel grade, (c, d) CG-HAZ after PWHT (700°C, 2 h), and (e, f) 42CrMo4_1200-700 steel grade

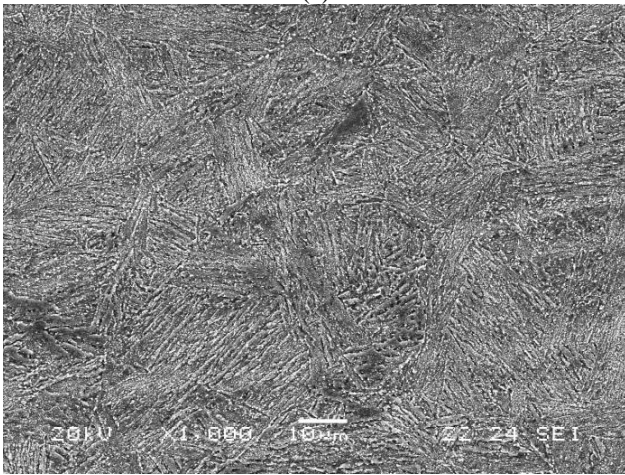
The average HV_1 microhardness values measured in the CG-HAZ produced after the deposition of the weld bead was 571, which corresponds to a fully martensitic microstructure of the 42CrMo4 steel. This microstructure is shown in Fig. 4 (a, b). Although a small percentage of bainite was found, the microstructure is mainly martensitic. After the post-welding heat treatment (tempering at 700°C for 2h), the average HV_1 microhardness determined on the CG-HAZ (PWHT) was 248. The pronounced drop in hardness is a direct consequence of the tempering of the martensite microstructure: internal stress relaxation, with profuse carbide precipitation, along with recovery and recrystallization phenomena affecting the martensite laths and packets. This microstructure is shown in Fig. 3 (c, d).



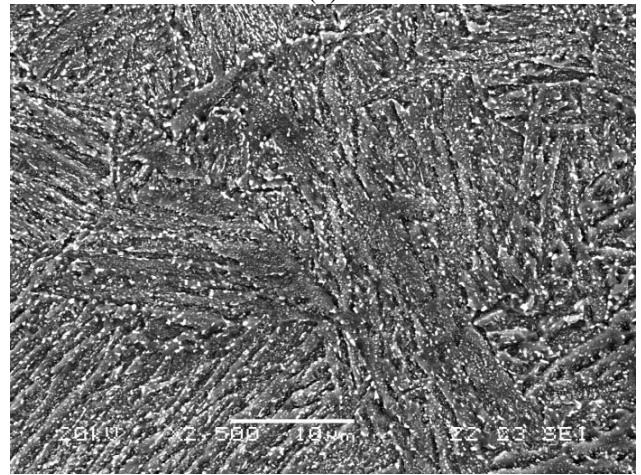
(a)



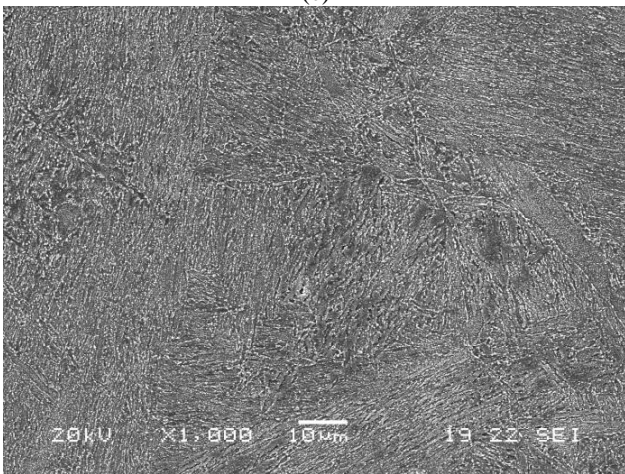
(b)



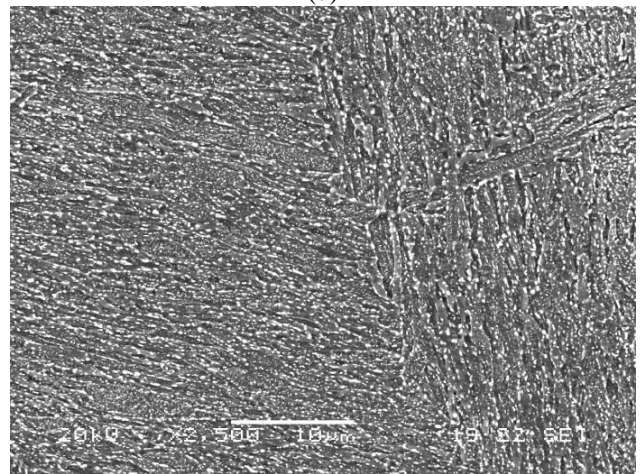
(c)



(d)



(e)



(f)

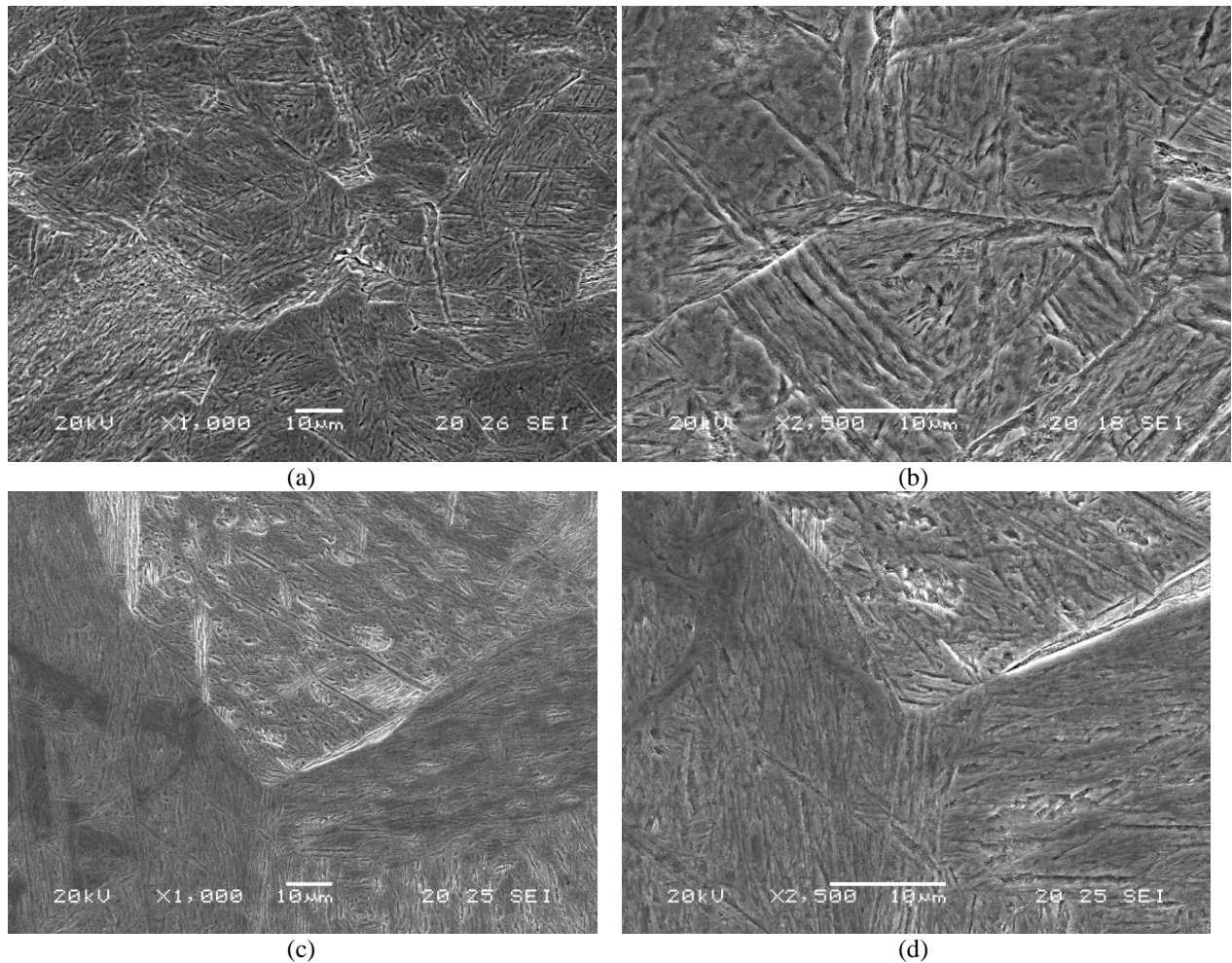


Fig. 4. SEM microstructures. (a, b) CG-HAZ, and (c, d) 42CrMo4_1200 steel grade

On the other hand, the average HV_{30} hardness measured in the steel after performing the simulated heat treatment designed to reproduce the CG-HAZ weld microstructure (1200°C/20min+oil quenching) was 585. This value is very similar to that measured in the CG-HAZ obtained close to the fusion line after the deposition of the weld bead, as can be observed in Table 3. Fig 4 (c, d) shows the obtained microstructure, consisting of nearly 100% martensite (with a small percentage of bainite). Using Vilella's reagent etching, an average prior austenite grain size of 150 µm was measured in this steel grade (coarse-grained).

Finally, the value of the HV_{30} hardness measured in this steel grade after the post-welding heat treatment (700°C/2h), 42CrMo4_1200-700, was 230 (very similar to the hardness value measured in the CG_HAZ after the PWHT, Table 3). The microstructure is shown in Fig. 3 (e, f). The profuse, uniformly distributed carbide precipitation that takes place during the high temperature tempering (700°C/2h) throughout the microstructure of the steel can be clearly observed in this figure.

Based on the results shown in Table 3, along with the microstructures shown in Figs. 3 and 4, it is worth noting that we have successfully reproduced the CG-HAZ generated in the deposition of a weld bead onto pieces of 42CrMo4 steel with a relatively high volume (simulated treatment). Moreover, after the application of a PWHT similar to the tempering treatment applied to the base steel (700°C for 2 h), a similar microstructure to that of the fine-grained base steel was obtained, as well as similar hardness values.

The behaviour versus hydrogen embrittlement of the base steel, the fine-grained steel (42CrMo4_845-700) and the simulated CG-HAZ after PWHT (42CrMo4_1200-700), with a coarser prior austenite grain size, are compared in the following sections. Both microstructures were very similar (tempered martensite),

except for the austenitic grain size, 20 μm in the fine-grained base steel and 150 μm in the coarse-grained steel (simulated CG-HAZ).

Weld	CG-HAZ	Hardness, HV ₁
CG-HAZ 42CrMo	CG-HAZ	571 \pm 40
CG-HAZ+PWHT	CG-HAZ+ 700°C/2h	248 \pm 6
Simulated CG-HAZ	Heat treatment	Hardness, HV ₃₀
42CrMo4_1200	1200°C/20min	585 \pm 9
42CrMo4_1200-700	1200°C/20min + 700°C/2h	230 \pm 2
Base steel	Heat treatment	Hardness, HV ₃₀
42CrMo4_845	845°C/45min	535 \pm 6
42CrMo4_845-700	845°C/45min+700°C/2h	207 \pm 2

Table 3. 42CrMo4 hardness results. CG-HAZ weld, simulated CG-HAZ and base steel

3.2 Hydrogen embrittlement study. Comparison between fine-grained and coarse-grained steels

3.2.1 Hydrogen uptake and hydrogen desorption curves

The hydrogen desorption curves at room temperature, obtained with the 42CrMo4_845-700 (fine-grained) base steel and the simulated CG-HAZ, 42CrMo4_1200-700 (coarse-grained) steel, are shown in Fig. 5 (the numerical fits used to calculate the apparent hydrogen diffusion coefficient are also reported in the same figure). The initial hydrogen content, C_0 , was respectively 1.2 and 1.0 ppm in the fine-grained and coarse-grained steels. As the hydrogen content measured in these steel grades before hydrogen charging was 0.1 ppm, a significant hydrogen uptake thus took place during the charging process. The desorption results obtained with the two 42CrMo4 steel grades are summarized in Table 4, along with the numerically estimated hydrogen diffusion coefficient, D_{app} .

As previously mentioned, data fitting of the experimentally determined desorption data was used to estimate the apparent hydrogen diffusion coefficient, D_{app} , in both steel grades. As an example, the homogeneous hydrogen concentration at the end of hydrogen pre-charging is shown in Fig. 6(a) and the initial hydrogen distribution at the end of the cooling phase (from 450 to 85°C performed in the high pressure reactor) in the case of the 42CrMo4_845-700 steel is also shown in Fig. 6(b). This hydrogen distribution corresponds to the first data point of the desorption curve, where an average hydrogen content of 1.2 ppm was experimentally measured. However, at this moment the specimen surface retains the deep trapped hydrogen concentration (0.3 ppm in this steel grade, which represents our surface boundary condition), but a hydrogen content as high as 2.2 ppm is still present in the centre of the specimen. Fig. 6(c) corresponds to the final situation, after a sufficiently long time at room temperature, where all the sample has the deep trapped hydrogen concentration (0.3 ppm in this steel grade). The diffusion coefficient which provides the best fit to the experimental data was taken as the apparent diffusion coefficient of the steel.

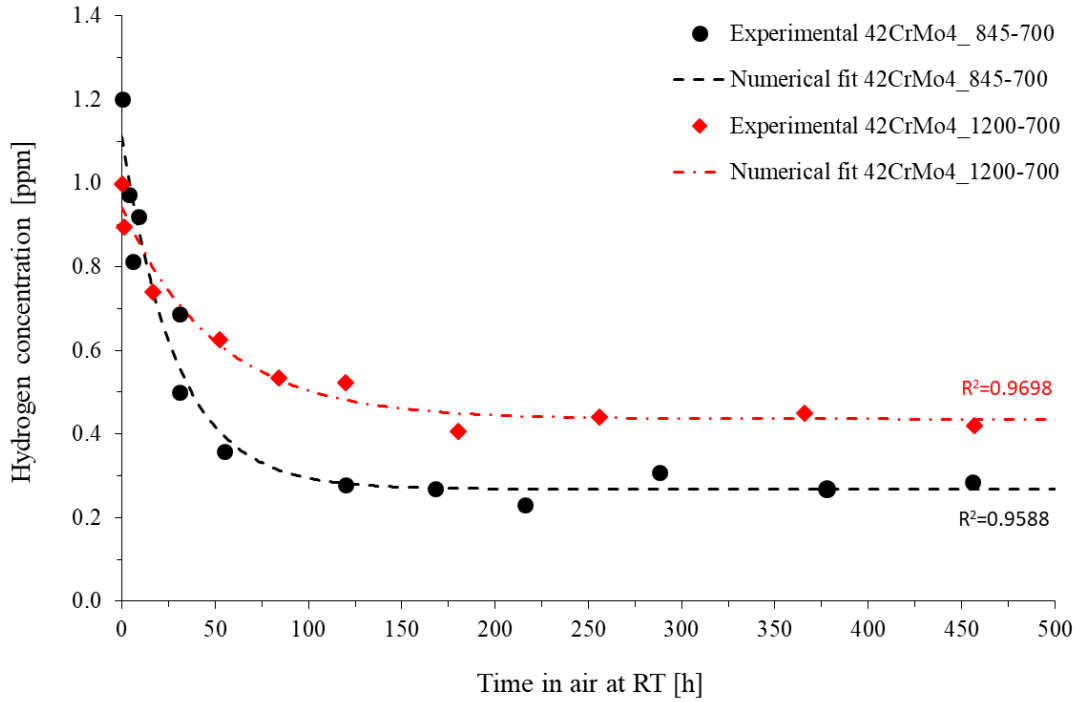


Fig. 5. Hydrogen desorption curves of the 42CrMo4_845-700 and 42CrMo4_1200-700 steel grades at room temperature and numerical fitting using Abaqus.

Steel Grade	HV ₃₀	PAGS [μm]	C ₀ [ppm]	C _{dt} [ppm]	C _{diff} [ppm]	D _{app} [m ² /s]
42CrMo4_845-700	207	20	1.2	0.30	0.90	4.34 10 ⁻¹⁰
42CrMo4_1200-700	230	150	1.0	0.45	0.55	2.51 10 ⁻¹⁰

Table 4. Initial (C₀), deep trapped (C_{dt}) and diffusible (C_{diff}) hydrogen content. Hydrogen diffusion coefficient (D_{app}) of the two 42CrMo4 steel grades.

When the austenitizing temperature increases from 845 to 1200°C, a significant increase in the prior austenite grain size occurs (from 20 to 150 μm), a similar increase in martensite lath and packet sizes also takes place and the initial hydrogen content decreases from 1.2 to 1 ppm. These results can be explained in terms of trapping phenomena in the prior austenitic grain and martensitic lath boundaries, where profuse carbide precipitation (Fe- and Cr-rich carbides [41]) takes place during tempering, as shown in Fig. 3. When the size of the aforementioned features increases, the density of the austenitic grain boundaries and lath interfaces decreases, as does the accumulated hydrogen content in these regions. Moreover, all these interfaces act as weak hydrogen traps, with activation trapping energies below 20 kJ/mol [42-46]. Hence, a major fraction of the initial hydrogen trapped in these traps will escape when kept at room temperature.

On the other hand, the final hydrogen content, C_{dt}, which represents the deep trapped hydrogen, comprises the hydrogen strongly trapped and retained in the steel microstructure after a long time at room temperature (more than a month in this case). The value of C_{dt} was greater in the 42CrMo4_1200-700 steel grade, 0.45 ppm versus 0.3 ppm, a result that can be attributed to the higher hardness of this steel grade (230 HV) compared to the base steel (207 HV). In quenched and high temperature tempered medium-carbon low-alloyed steels like this one, most of the deep trapped hydrogen concentrates along dislocations, generated during the quenching stage. The greater thermal drop applied to quench the 42CrMo4_1200-700 steel grade (quenched from 1200°C, instead of 845°C in the case of the base steel) gives rise to a more distorted martensitic structure, with higher internal stresses and hence a higher dislocation density [47]. A similar explanation likewise justifies the slightly lower value of the hydrogen diffusion coefficient calculated with

the coarse-grained steel ($2.51 \times 10^{-10} \text{ m}^2/\text{s}$) compared to the fine-grained base steel ($4.34 \times 10^{-10} \text{ m}^2/\text{s}$), shown in Table 4.

The diffusible hydrogen content, C_{diff} , (i.e. the difference between the initial and the deep trapped hydrogen content ($C_0 - C_{\text{dt}}$), which is the hydrogen able to move freely within the steel microstructure at room temperature, overcome traps and escape from the steel) is substantially higher in the fine-grained base steel, once again demonstrating that the density of weak traps ($E_a < 30 \text{ kJ/mol}$) is greater in this case.

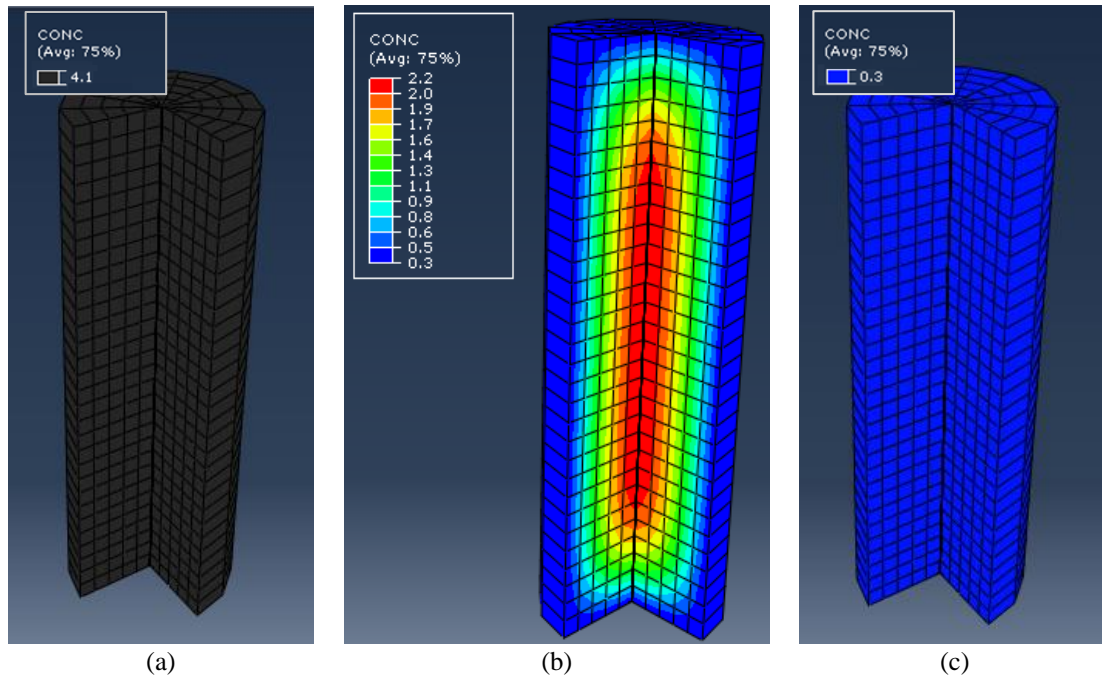


Fig. 6. Hydrogen distribution (ppm) in the 42CrMo4_845-700 steel cylindrical samples ($R=5\text{mm}$ and $L=30\text{mm}$). (a) Homogeneous hydrogen concentration at the end of the pre-charge. (b) Distribution of hydrogen in the specimen at the beginning of the desorption curve at RT (average hydrogen concentration of 1.2 ppm). (c) Deep trapped hydrogen concentration (0.3 ppm) after 48 h at RT.

3.2.2 Tensile tests on smooth specimens

Table 5 shows the results obtained in the tensile tests performed on smooth, uncharged and hydrogen pre-charged, specimens of 42CrMo4 fine and coarse-grained steels. The values of the embrittlement indexes associated with the different mechanical properties obtained in these tests are also included in this table, along with the test duration. Additionally, Figs. 7 and 8 respectively show the stress-strain curves obtained with both steel grade, uncharged and hydrogen pre-charged.

In the absence of hydrogen, the steel with the largest austenitic grain size (42CrMo4_1200-700) exhibits a slightly higher strength, justified by its greater hardness. However, the ductility parameters were approximately similar in both steel grades.

Steel grade	v_{test} [mm/min]	Test duration [h]	σ_{ys} [MPa]	σ_{ut} [MPa]	A [%]	Z [%]	$EI_{(\sigma_{\text{ys}})}$ [%]	$EI_{(\sigma_{\text{ut}})}$ [%]	$EI_{(A)}$ [%]	$EI_{(Z)}$ [%]
845-700 (20 μm , 207 HV)	0.4	0.33	622	710	22.6	61.3	-	-	-	-
	0.4	0.35	585	694	21.6	64.2	5.9	2.2	4.4	0
	0.04	2.7	590	689	21.7	62.6	5.1	3.0	4.0	0
1200-700 (150 μm , 230 HV)	0.4	0.35	600	750	23.6	65.5	-	-	-	-
	0.4	0.35	610	755	22.5	67.8	0	0	4.7	0
	0.04	3.3	593	731	20.2	67.6	1.2	2.5	14.4	0
	0.004	29.4	580	710	18.1	65.7	3.3	5.3	23.3	0

Table 5. Results of the tensile tests performed at different displacement rates on smooth specimens of the 42CrMo4_845-700 and 42CrMo4_1200-700 steel grades, uncharged and hydrogen pre-charged

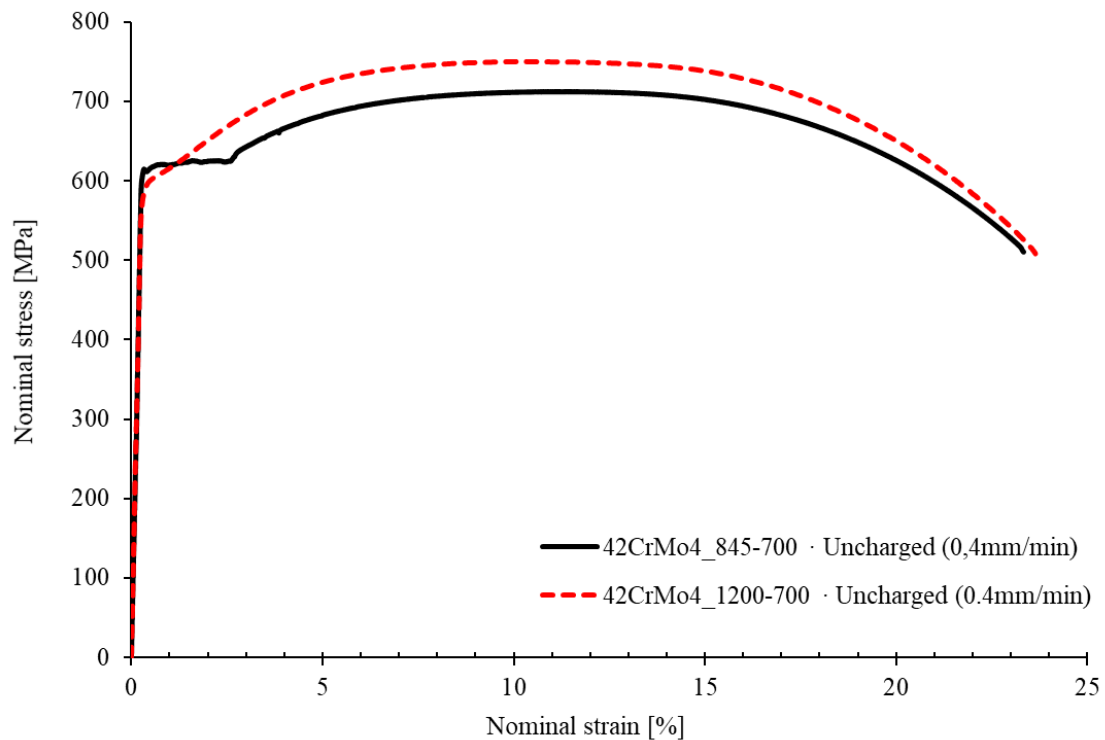


Fig. 7. Engineering stress-strain curves obtained with smooth tensile specimens (0.4 mm/min) of the uncharged 42CrMo4_845-700 and 42CrMo4_1200-700 steel grades

In the case of the base steel (Fig. 8(a)), with a smaller prior austenite grain size and lower hardness, minor differences were detected between tests carried out on uncharged and hydrogen pre-charged specimens regardless of the applied displacement rate. In this case, all the embrittlement indexes remained below 6%. However, in the case of the coarse-grained steel (Fig. 8(b)), although the effects of HE were also negligible in terms of yield strength and ultimate tensile strength, a certain reduction in ductility was observed, specifically reflected in the final elongation. In fact, the embrittlement index associated with this parameter, $EI_{(A)}$, gradually increases as the displacement rate decreases, reaching a value of over 20% for the test performed at the lowest displacement rate, 0.004 mm/min.

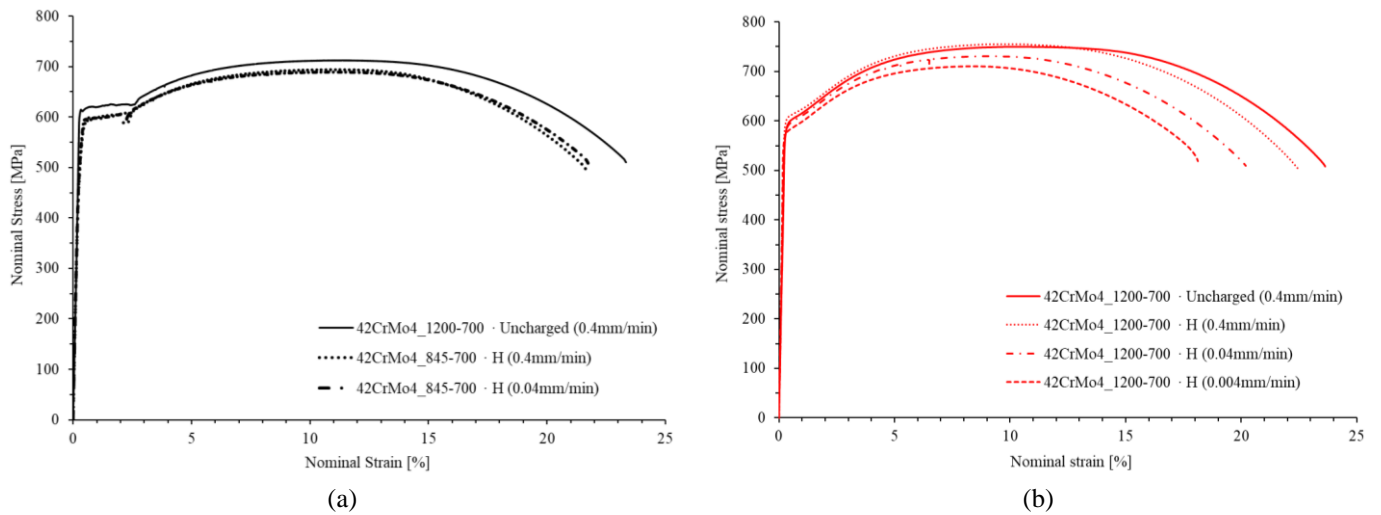


Fig. 8. Engineering stress-strain curves obtained with smooth tensile specimens of uncharged and hydrogen pre-charged specimens, (a) 42CrMo4_845-700 and (b) 42CrMo4_1200-700 tested at different strain rates

3.2.2.1. Fracture surfaces analysis of the smooth tensile specimens

The fracture micromechanism observed by means of SEM in the failure surfaces of the smooth tensile specimens of both steel grades tested without hydrogen was always fully ductile, being characterized by microvoid coalescence (MVC), as can be seen in Fig. 9.

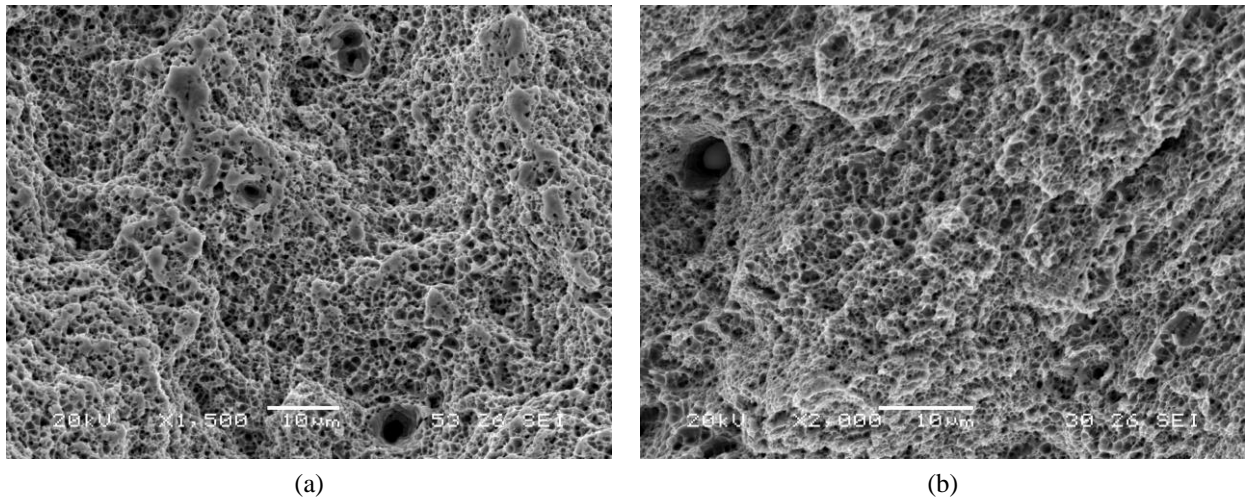


Fig. 9. Fracture micromechanism of smooth uncharged tensile specimens (a) 42CrMo4_845-700, and (b) 42CrMo4_1200-700.

No significant change in the failure micromechanism was observed in the fracture surface of the tensile specimens of either steel grade tested under internal hydrogen. Fig. 10 shows the fracture mechanism of 42CrMo4_1200-700 steel tested with internal hydrogen under the lowest displacement rate (0.004 mm/min), where maximum embrittlement indexes were observed. Microvoid coalescence (MVC) is the only failure micromechanism detected in the entire fracture surface.

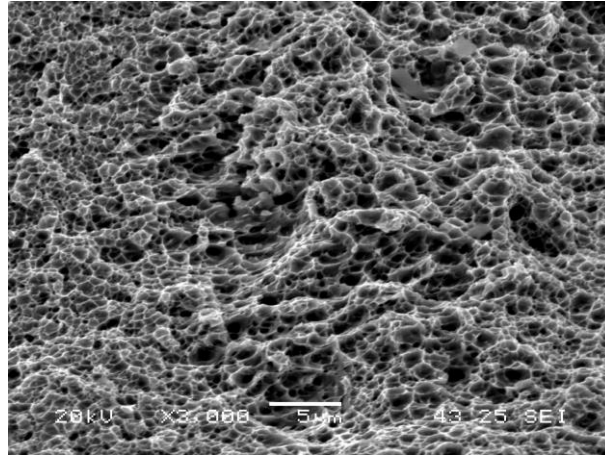


Fig. 10. Fracture micromechanism of smooth tensile specimens of 42CrMo4_1200-700, hydrogen pre-charged and tested at 0.004 mm/min

3.2.3. Tensile tests on notched specimens

The stress-strain curves obtained with uncharged and hydrogen pre-charged notched specimens ($k_t=4.3$) of both steel grades (fine- and coarse-grained) tested at different displacement rates (0.4 mm/min in the case of the uncharged samples and 0.4, 0.04, 0.004 and 0.002 mm/min for the H-charged ones) are shown in Fig. 11.

It is now worth noting that, as the test displacement rate decreases, ductility considerably decreases, especially in the case of the steel grade with coarser grain size (42CrMo4_1200-700). Under the slowest test displacement rate (0.002 mm/min), however, the negative effect of hydrogen seems to finally stabilize.

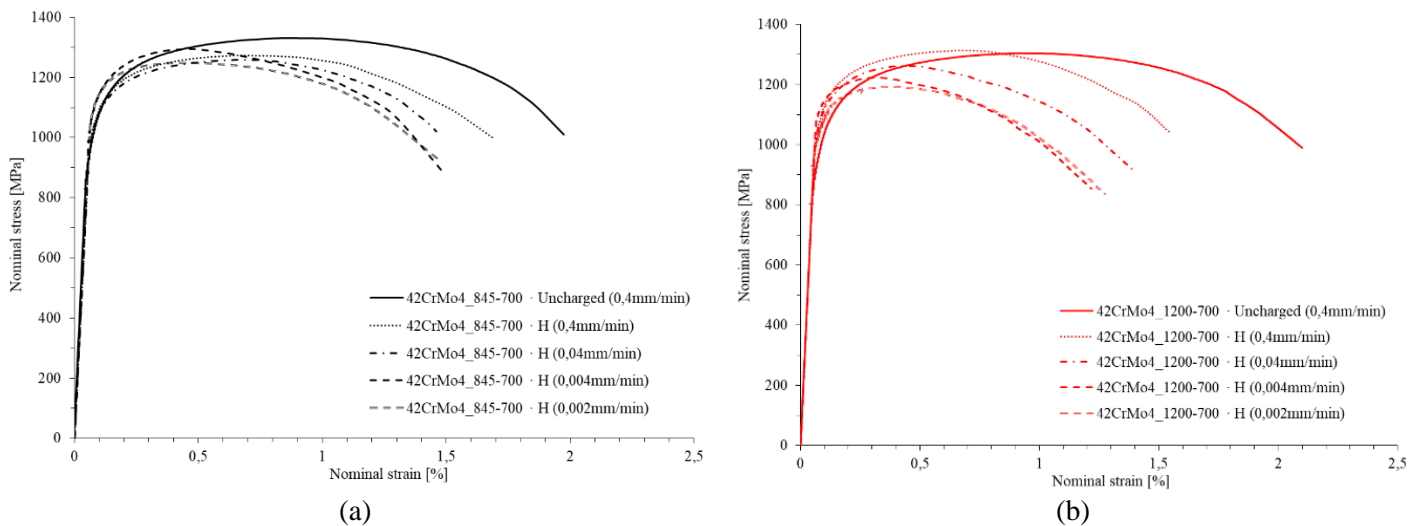


Fig. 11. Engineering stress-strain curves of the uncharged and hydrogen pre-charged notched tensile specimens ($k_t=4.3$) of a) 42CrMo4_845-700 and b) 42CrMo4_1200-700 steel. Influence of the applied displacement rate.

Additionally, Table 6(a) shows the values obtained for the notch tensile strength (σ_N), elongation at failure (ϵ_{max}) and reduction in area (RA) using uncharged and hydrogen pre-charged specimens under different displacement rates. The embrittlement indexes calculated for the aforementioned mechanical properties, test duration and the approximate evolution of the average hydrogen content (C_H) in the specimens

throughout the course of the test are also included in the table. It is worth noting that the test duration barely affected the hydrogen content in these specimens, except at the lowest displacement rates. Nonetheless, the values of C_H in Table 6 should be taken with caution, as they were derived from the desorption curves (Fig. 5) and the dimensions of the two types of specimens were not the same. Moreover, local hydrogen concentrations are expected to be much greater in the region close to the notch tip, where the hydrostatic stress reaches maximum values [27, 48]. Furthermore, the prevailing fracture micromechanisms (and their extension into the failed surface), which will be fully analysed in the next section, are also presented in Table 6(b).

Steel Grade	V_{test} [mm/min]	Test duration [h]	C_H [ppm]	σ_N [MPa]	ϵ_{max} [%]	RA [%]	$EI_{(\sigma_N)}$ [%]	$EI_{(\epsilon_{max})}$ [%]	$EI_{(RA)}$ [%]
845-700 (20 μ m, 207HV)	0.4	0.20	-	1330	1.97	12.5	-	-	-
	0.4	0.15	1.2	1273 \pm 21	1.68	11.8 \pm 0.1	4.3	14.7	5.6
	0.04	1.3	1.2 \rightarrow 1.1	1258 \pm 20	1.46	10.3 \pm 1.6	5.4	25.9	17.9
	0.004	13.5	1.2 \rightarrow 0.8	1294	1.48	9.6	2.7	24.9	23.1
	0.002	35.9	1.2 \rightarrow 0.5	1250 \pm 61	1.48 \pm 0.3	9.8 \pm 0.6	6.1	24.9	21.2
1200-700 (150 μ m, 230HV)	0.4	0.22	-	1304	2.1	13.3	-	-	-
	0.4	0.18	1.0	1313	1.6	10.8	0	23.8	18.5
	0.04	1.6	1.0 \rightarrow 0.9	1238 \pm 35	1.4	8.7 \pm 0.8	5.8	33.3	34.8
	0.004	13.3	1.0 \rightarrow 0.8	1206 \pm 23	1.2	7.4 \pm 0.3	8.3	42.9	44.2
	0.002	25.7	1.0 \rightarrow 0.7	1193	1.3	6.1	9.3	38.1	54.0

(a)

Steel Grade	V_{test} [mm/min]	C_H [ppm]	Fracture Micromechanisms*	
			Periphery	Bulk
845-700 (20 μ m, 207HV)	0.4	-	MVC	
	0.4	1.2	MVC	
	0.04	1.2 \rightarrow 1.1	MVC (elongated)	
	0.004	1.2 \rightarrow 0.8	CMD (175 μ m)	MVC (elongated)
	0.002	1.2 \rightarrow 0.5	MLD (20 μ m) + CMD (120 μ m)	MVC (elongated)
1200-700 (150 μ m, 230HV)	0.4	-	MVC	
	0.4	1.0	MLD (10 μ m) + CMD (150 μ m)	MVC (elongated)
	0.04	1.0 \rightarrow 0.9	MLD (10 μ m) + CMD (165 μ m)	MVC (elongated)
	0.004	1.2 \rightarrow 0.8	MLD (75 μ m) + IG (250 μ m)	MVC (elongated)
	0.002	1.2 \rightarrow 0.7	MLD (75 μ m) + IG (375 μ m)	MVC (elongated)

(b)

Table 6. (a) Results of tensile tests performed on notched specimens ($Kt=4.25$) of uncharged and hydrogen pre-charged 42CrMo4_845-700 and 42CrMo4_1200-700 steel grades loaded at different displacement rates. (b) Operative fracture micromechanisms throughout the tests. *MVC: microvoid coalescence; CMD: carbide-matrix interface decohesion; MLD: martensitic lath interface decohesion; IG: intergranular fracture

Fig. 12 provides a summary of all these results. It shows the embrittlement indexes, EI, for the reduction in area (RA), maximum deformation (ϵ_{max}) and notch strength (σ_N) for hydrogen pre-charged notched tensile specimens of both steel grades versus the applied displacement rate.

First, it is worth noting that the steel with the coarsest grain size suffered the greatest embrittlement in all cases. Moreover, only a slight decrease in the notched strength can be appreciated in both steel grades for displacement rates lower than 0.4 mm/min: this embrittlement index remained almost constant and always below 10%. As stated previously, the properties related to ductility were those most affected by hydrogen.

In fact, the embrittlement index related to the reduction in area, $EI_{(RA)}$, reached values of over 20% and 50% for the finer and coarser grain size steels, respectively, when tested under the lowest displacement rates.

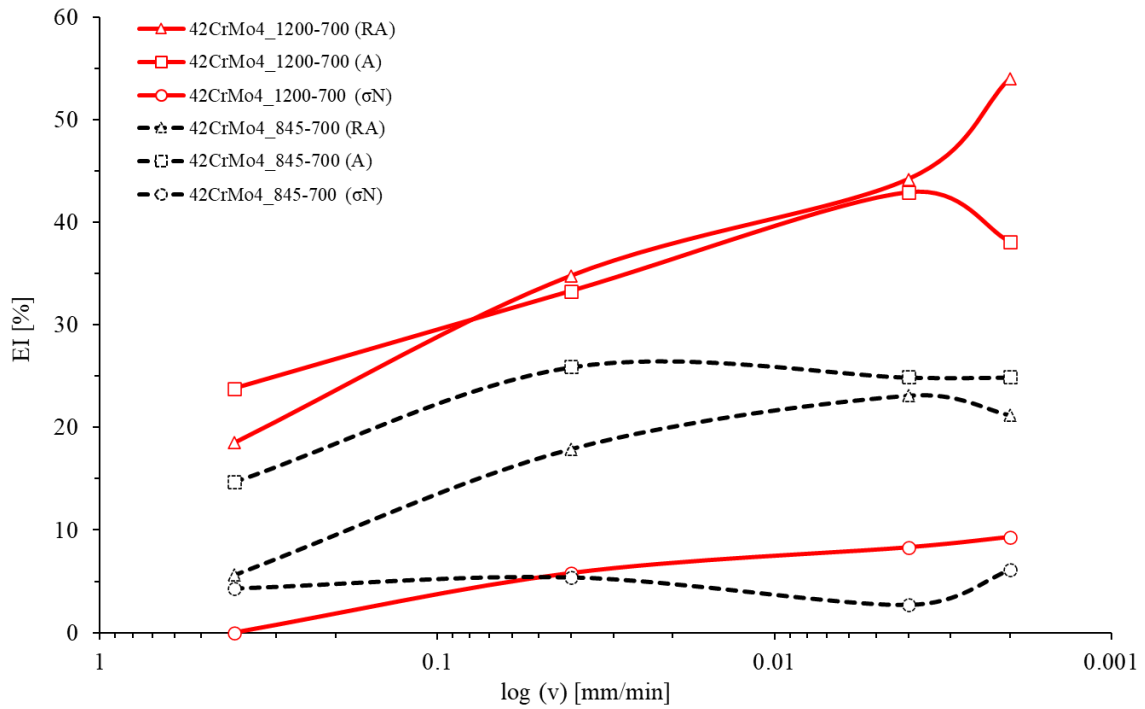


Fig. 12. Embrittlement indexes associated with the reduction in area (RA), maximum elongation (ϵ_{max}) and notch strength (σ_N) versus displacement rate. Hydrogen pre-charged notched tensile specimens.

3.2.3.1. Fracture surface analysis of notched tensile specimens

The fracture surfaces corresponding to the notched tensile specimens of both steel grades were analysed using SEM and the main operative fracture micromechanisms were identified.

At first, the fracture micromechanism of both steel grades tested without internal hydrogen was fully ductile, characterized by microvoid coalescence (MVC), as can be seen in Fig 13(a, b) for the coarse-grained steel.

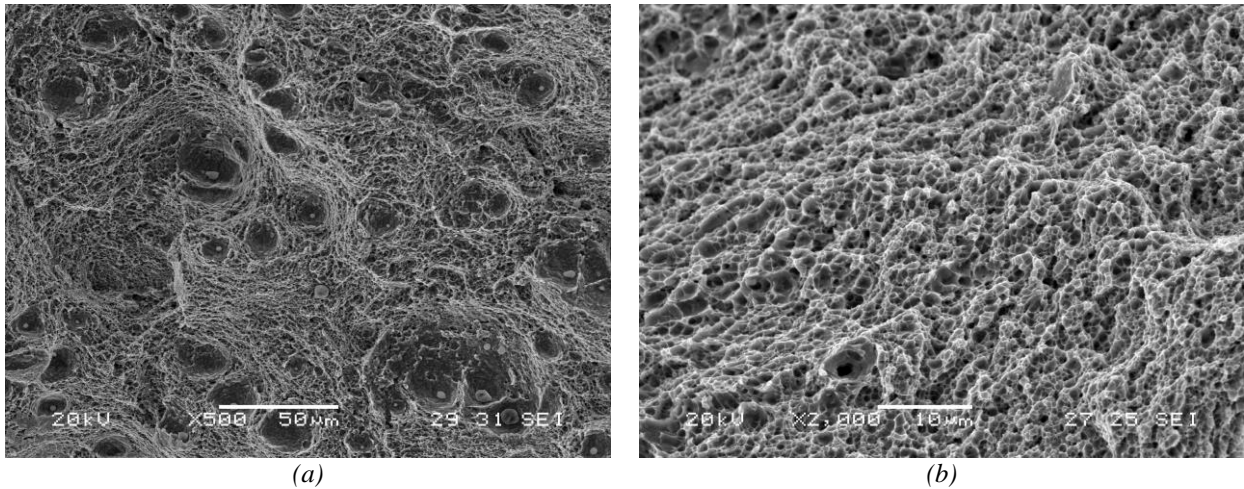


Fig. 13. Fracture micromechanism of uncharged 42CrMo4_1200-700 at different magnifications.

As to the fine-grained base steel (42CrMo4_845-700), Fig. 14 shows the fracture surfaces of the notched tensile specimens tested with internal hydrogen at different displacement rates. In the case of the fastest test, carried out at the same displacement rate as that used with the uncharged specimens (0.4 mm/min), hydrogen has not modified the operative fracture micromechanism, which is still MVC (see Fig. 14(a)). However, when the applied displacement rate was 10 times lower (0.04 mm/min), the effects of hydrogen begin to appear in the form of flattened and elongated areas, like those indicated by black arrows in Fig. 14(b). These flattened and elongated areas are generally associated with strain localization ahead of the notched region due to local accumulation of hydrogen, following the mechanism described as hydrogen enhanced localized plasticity (HELP) [49-51]: the accumulation of hydrogen in front of the notch, due to the high triaxiality existing in this region, facilitates dislocation movement, plastic deformation localised and extended, giving rise to shallow and elongated dimples.

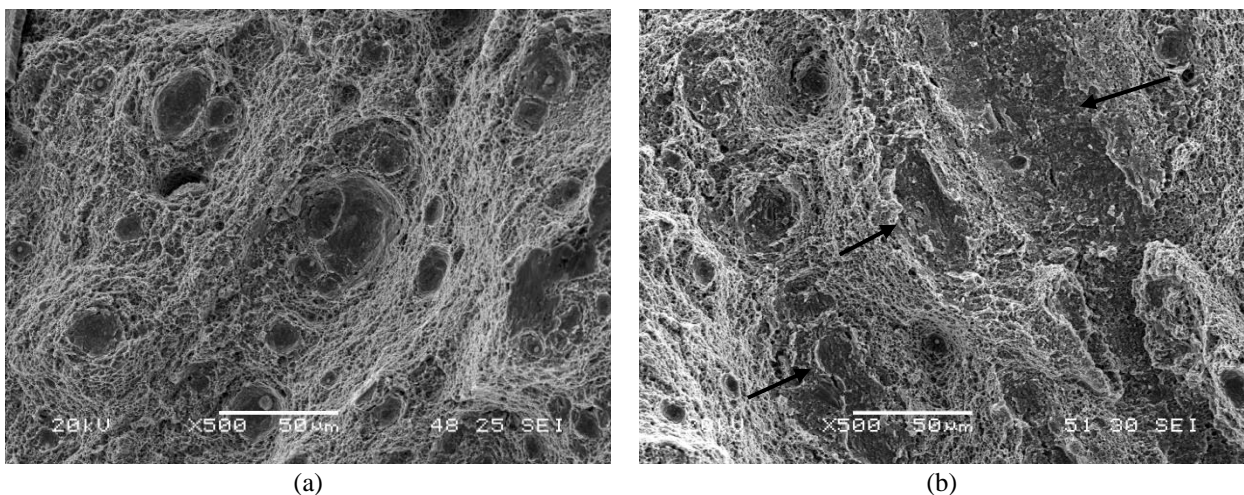


Fig. 14. Fracture micromechanism of notched tensile specimens of the base steel grade (42CrMo4_845-700) tested with internal hydrogen at (a) 0.4 mm/min, and (b) 0.04 mm/min

Moreover, when the specimens were tested with internal hydrogen at a displacement rate 100 times lower (0.004 mm/min), apart from the presence of elongated microvoids in the bulk of the specimen (Fig. 15(a)), a narrow band in the periphery ahead of the notch (with an average extension of about 175 µm)

characterized by a flatter topography can be observed (Fig. 15(b, c)). A closer look at this area (Fig. 15(d)) revealed the presence of very small microvoids, with an approximate diameter of around 0.5 μm . These microvoids are produced by decohesion along matrix-carbide interfaces, a micromechanism denominated carbide-matrix interface decohesion (CMD) in this study, which is promoted by a high local hydrogen concentration in these particular interfaces (weak hydrogen traps).

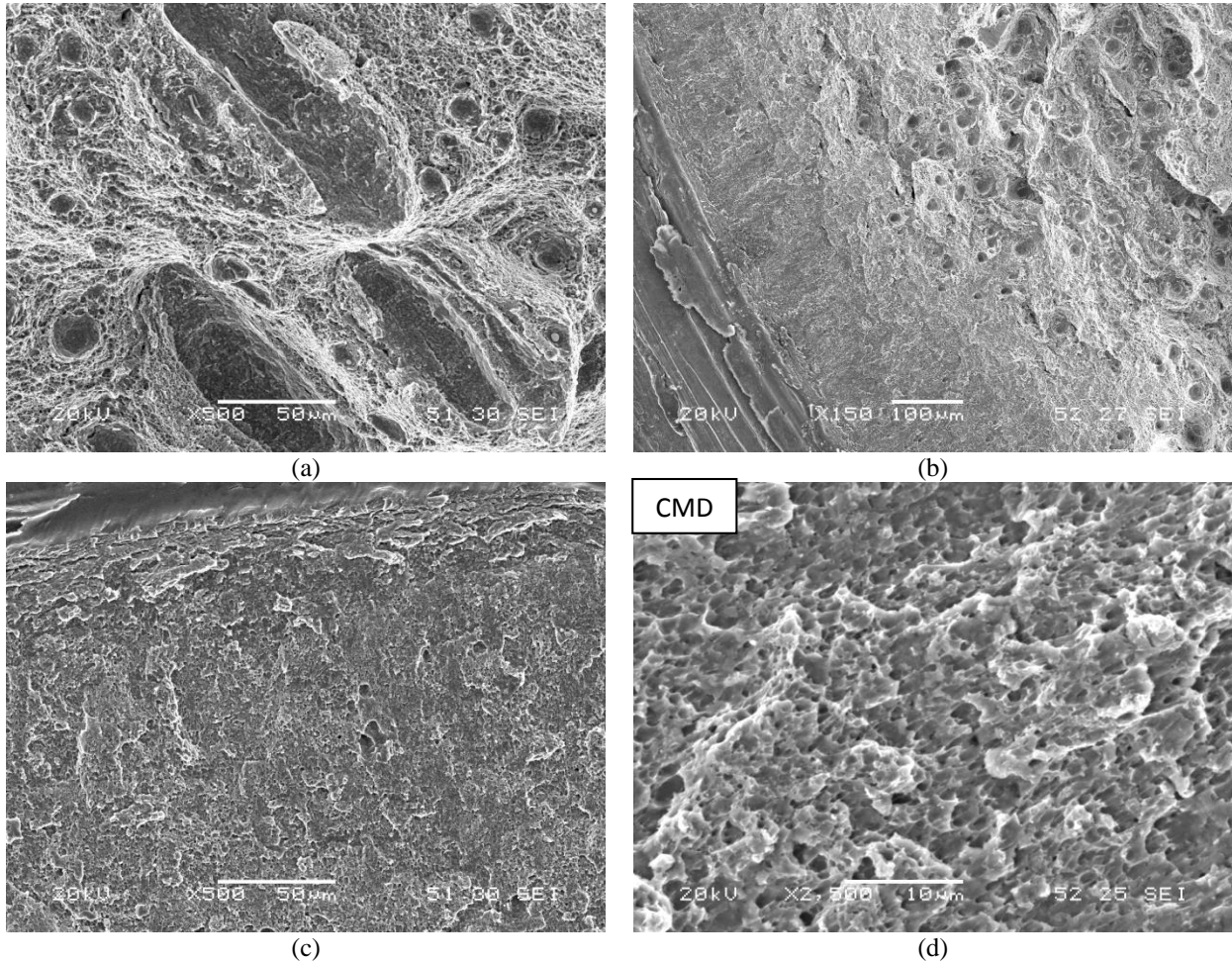


Fig. 15. Fracture micromechanism of notched tensile specimens of the base steel grade (42CrMo4_845-700) tested with internal hydrogen at 0.004 mm/min. (a) Elongated microvoids in the bulk of the specimen, and (b, c, d) CMD (carbide-matrix interface decohesion) fracture in the periphery

Fractographs of the specimens tested at the lowest displacement rate (0.002 mm/min) are shown in Fig. 16. Once again, elongated microvoids in the bulk of the specimens (Fig. 16(a)) and a peripheral belt of approximately 120 μm characterized by CMD (Fig. 16(b, c, d)) were clearly observed. Additionally in this case, a narrow band of around 20 μm , shown in Fig. 16(e), characterized by decohesion along martensitic lath boundaries, called martensitic lath decohesion (MLD) in this study, was found in the most peripheral region of the specimen, just ahead of the notch tip. The use of a lower displacement rate allows hydrogen to diffuse from the bulk through the most strained area of the specimen (in the vicinity of the notch tip [27, 48]). This hydrogen is trapped in this region at the martensitic lath interfaces, thus promoting their decohesion when a critical concentration is reached. This kind of fracture micromechanism is sometimes also referred to as plasticity-related hydrogen induced cracking (PRHIC) in martensitic steels [45].

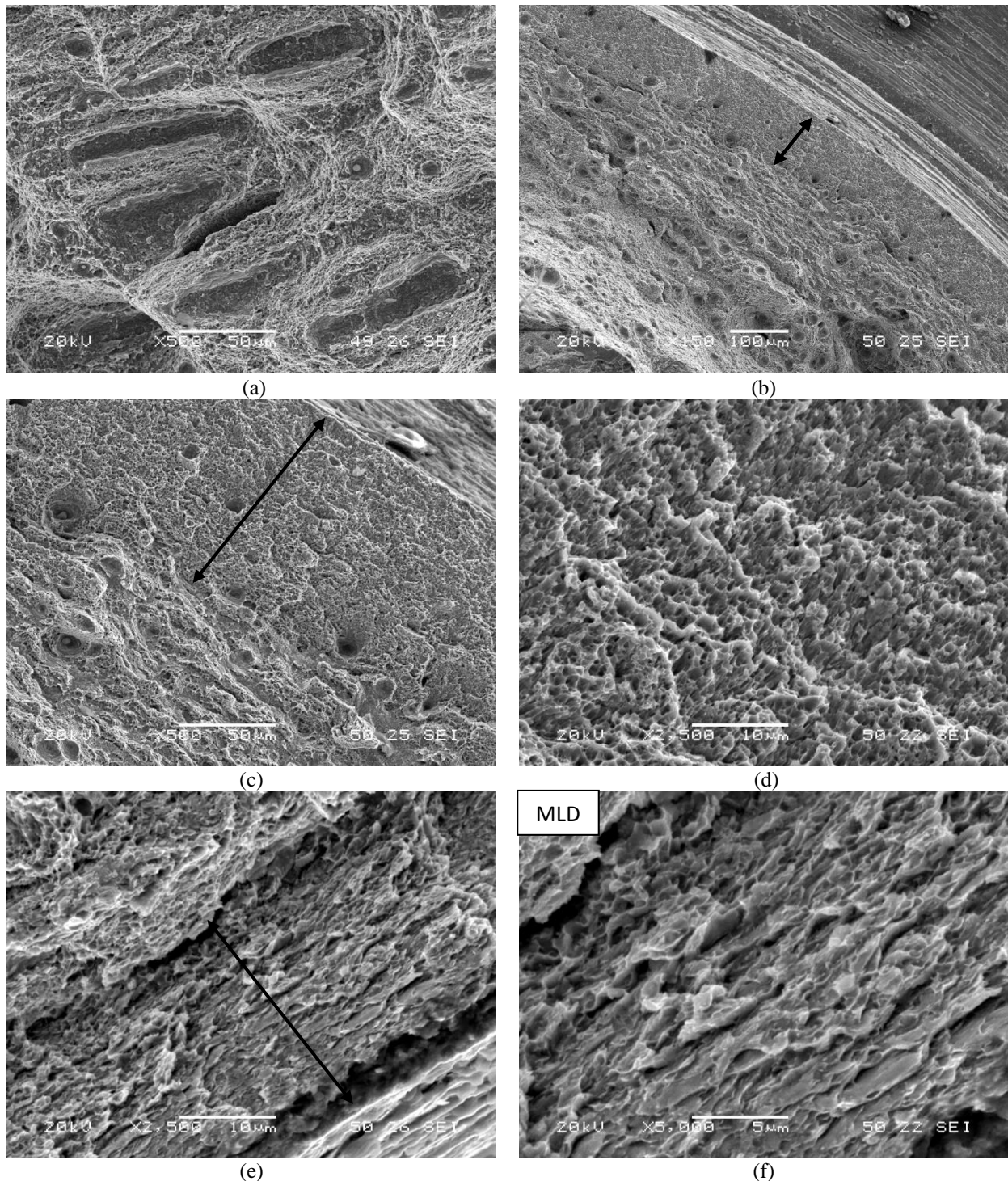


Fig. 16. Fracture micromechanism of notched tensile specimens of the base steel grade (42CrMo4_845-700) tested with internal hydrogen at 0.002 mm/min. (a) Elongated microvoids in the bulk of the specimen, (b, c, d) CMD (carbide-matrix interface decohesion) peripheral belt, and (e, f) MLD (martensitic lath decohesion) in the most peripheral region ahead of the notch tip

Similarly, the fracture surfaces observed into the notched specimens of the coarse-grained steel (42CrMo4_1200-700) tested with internal hydrogen at 0.4 mm/min are shown in Fig. 17. The bulk of the specimen was characterized by the MVC micromechanism, where elongated microvoids due to the HELP mechanism can be appreciated (black arrows in Fig. 17(a)). Moreover, a flattened peripheral area ahead of the notch tip with an extension of around 150 μm can also be seen in Fig. 17(b). Apart from the CMD

(carbide-matrix interface decohesion) area, detail A, Figure 17(c), a small belt (with an extension of about 10 μm) characterized by the decohesion of martensitic lath interfaces (MLD) was also observed (detail B, Figure 17(d)). Similar failure micromechanisms were also observed in the specimens tested at 0.04 mm/min.

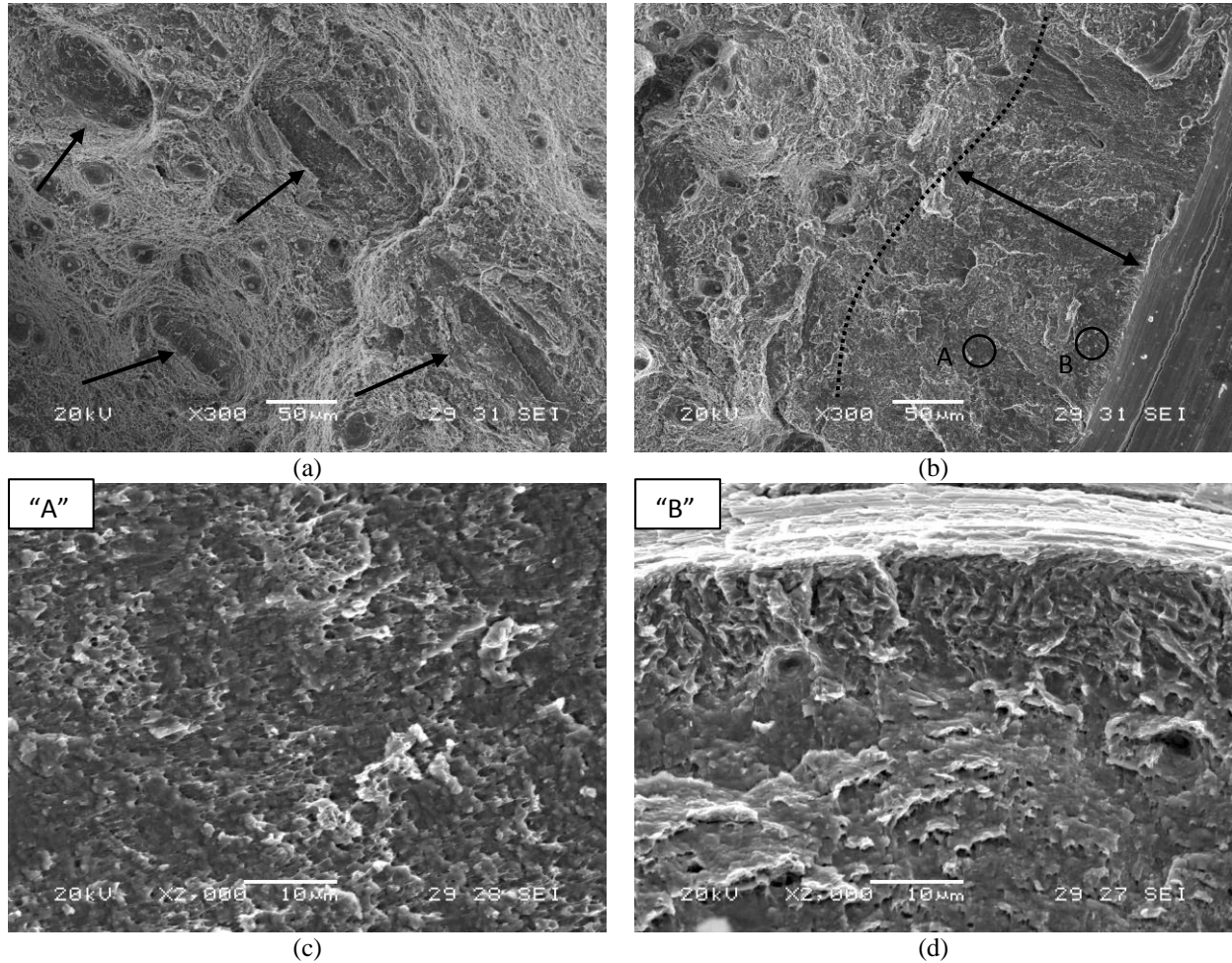


Fig. 17. Fracture micromechanism of notched tensile specimens of the 42CrMo4_1200-700 steel grade tested with internal hydrogen at 0.4 mm/min. (a) Elongated microvoids in the bulk of the specimen, (b, c) CMD (carbide-matrix interface decohesion) peripheral belt, and (d) MLD (martensitic lath decohesion) in the most peripheral region ahead of the notch tip

The fracture surfaces corresponding to the hydrogen pre-charged 42CrMo4_1200-700 notched tensile specimens tested at 0.004 mm/min are shown in Fig. 18 (similar failure micromechanisms were also observed at the lowest displacement rate of 0.002 mm/min). Yet again, as in the previous cases, the operative fracture micromechanism in the interior regions of the specimen was MVC with elongated and flat areas, as shown in Fig 18(a). A belt of around 50-100 μm in depth, characterized by decohesion along martensitic lath interfaces (MLD) as shown in Fig. 18(b, c, d), was detected in the periphery of the specimen (notch tip region). As expected, these martensitic laths are larger than those observed on the fine-grained base steel (see Figure 16(f)) due to the much greater austenitic grain size of the 42CrMo4_1200-700 steel grade. Moreover, intergranular fracture mechanisms (IG) were also active in some zones of the peripheral region, in an area of about 250 μm (see Fig. 18(e, f)). The estimated size of the grains directly measured on these fractographies was around 150-200 μm , which corresponds to the prior austenite grain size measured on the polished and etched sections of the steel.

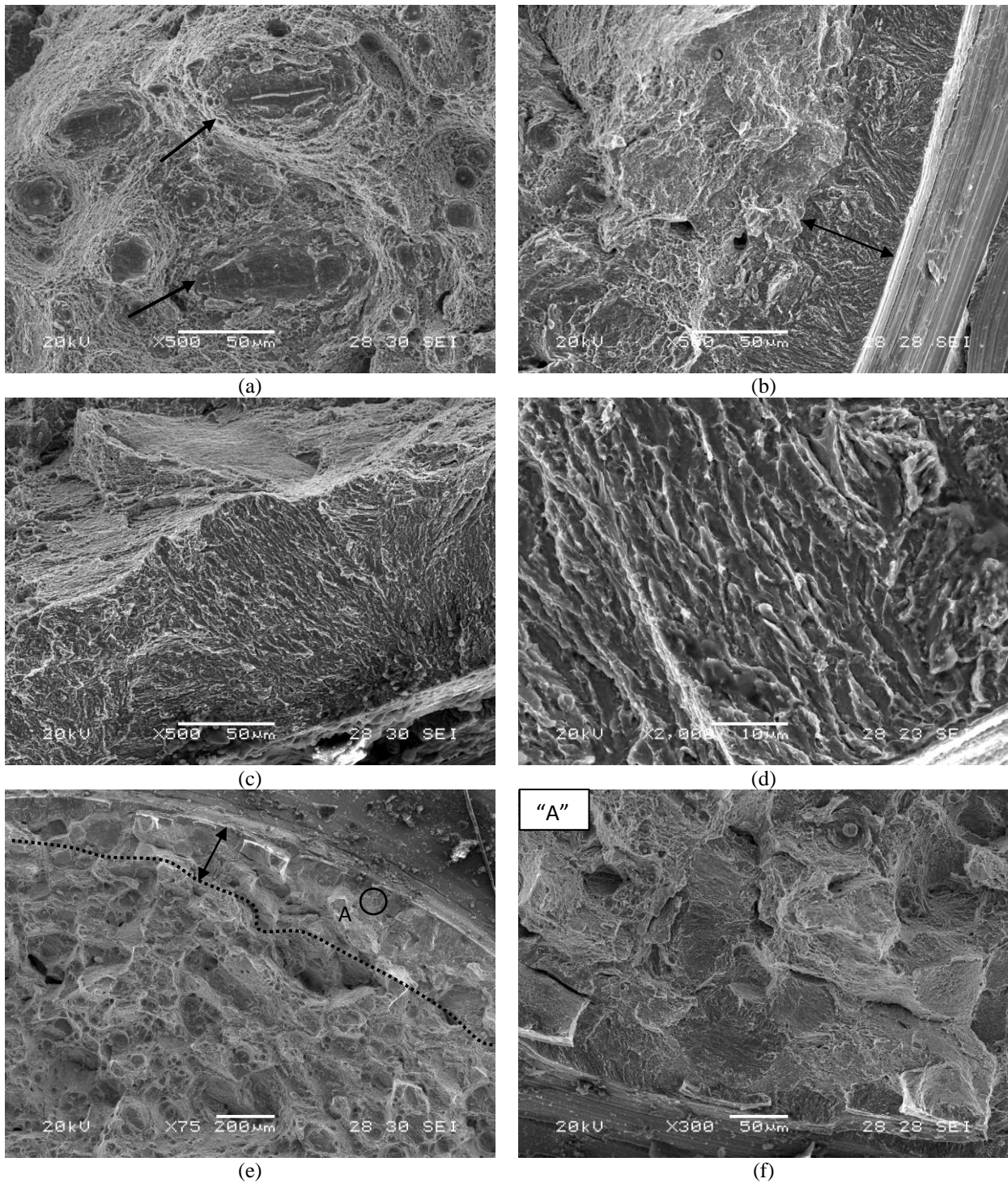


Fig. 18. Fracture micromechanism of notched tensile specimens of the 42CrMo4_1200-700 steel grade tested with internal hydrogen at 0.004 mm/min. (a) Elongated microvoids in the bulk of the specimen, (b, c, d) MLD (martensitic lath decohesion) in the most peripheral region ahead of the notch tip, and (e, f) IG fracture also active in some areas of the peripheral region

4. DISCUSSION

In order to explain the experimental results described in the previous section, the distribution of the local normal stress perpendicular to the notch plane, σ_{22} , the hydrostatic stress, σ_h , and the Von Mises stress, σ_{VM} , were obtained in the case of the fine-grained base steel at the moment of fracture of the tensile notched specimens. σ_h and σ_{VM} were respectively calculated according to Equations (7) and (8):

$$\sigma_h = \frac{\sigma_{11} + \sigma_{22} + \sigma_{33}}{3} \quad (7)$$

$$\sigma_{VM} = \sqrt{\frac{(\sigma_{11} - \sigma_{22})^2 + (\sigma_{22} - \sigma_{33})^2 + (\sigma_{33} - \sigma_{11})^2}{2}} \quad (8)$$

σ_{11} , σ_{22} and σ_{33} being the principal stresses.

A 2D axisymmetric elastic-plastic finite element model defined with a Hollomon hardening law ($\sigma_v = 1055 \epsilon_{plv}^{0.1264}$) was obtained from the tensile tests performed on smooth specimens in the absence of hydrogen (quite similar results were expected for the coarse-grained steel and also when internal hydrogen is introduced). The geometry of the specimen was unevenly meshed, this mesh being finer in the vicinity of the notch root. 8-node biquadratic axisymmetric quadrilateral elements with reduced integration (CAX8R) were used with a minimum size of around 40 μm .

Fig. 19 shows the distribution of σ_{22} , σ_h and σ_{VM} versus the distance from the notch tip at an applied stress equal to the notch tensile strength of the fine-grained base steel.

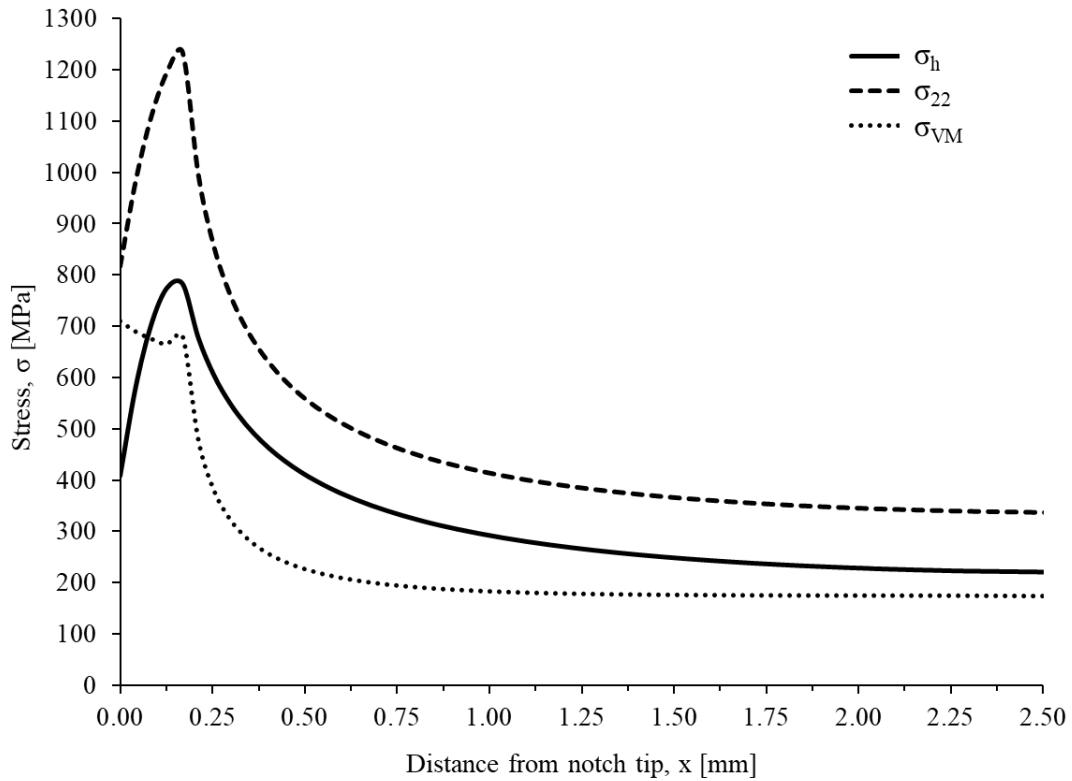


Fig. 19. Distribution of σ_h , and σ_{22} and σ_{VM} along the radial direction when the applied net stress is equal to the notch tensile strength. Base steel grade 42CrMo4_845-700 (fine-grained)

It is now well known that the internal hydrogen distribution in a steel with internal hydrogen submitted to an external load is governed by hydrostatic stress [27, 39, 45]. Hydrogen located in the surroundings of the notch tip will diffuse up to the process zone located just ahead of the notch root (driven by the high hydrostatic stress existing in this region, where it is trapped by dislocation entanglements produced in the plastic strained zone), where hydrogen atoms will accumulate and thereby give rise to embrittlement phenomena.

Returning to Figure 19, a plastic zone ($\sigma_{VM}/\sigma_{ys} > 1$) with a depth of 170 μm was predicted. Moreover, maximum values of both the normal stress and the hydrostatic stress are also predicted at a certain distance from the notch tip. Specifically, the maximal hydrostatic stress observed in Fig. 19 reaches 780 MPa at 170 μm from the notch tip and high hydrostatic stresses greater than the yield stress ($\sigma_{ys}=622$ MPa) are found at depths lower than 250 μm . The extension of the region submitted to high hydrostatic stress at the moment of failure of the different notched tensile specimens coincides quite well with the depth of the peripheral belt observed in those specimens in which hydrogen embrittlement micromechanisms (carbide-matrix interface decohesion, CMD, and intergranular fracture, IG) were observed (see Table 6 (b)). However, martensite lath interface decohesion, MLD, was observed to take place only at very low depths, in the first 20 and 75 μm , respectively, for the fine-grained and coarse-grained steels (Table 6 (b)) under the most demanding conditions (lowest displacement rates). At such small depths, within the plastic zone local plastic strain is maximal, dislocation density will have increased, hydrogen will accumulate on the dislocated martensite lath interfaces and this particular hydrogen embrittlement phenomenon takes place.

On the other hand, the available effective hydrogen diffusion distance, x_H , for the movement of hydrogen atoms during the tensile tests can be approximated by Equation (9), considering unidirectional hydrogen diffusion towards the notch root (hydrogen transport by dislocations from the bulk into the process zone was not taken into account). The following expression, in which D_{app} is the apparent hydrogen diffusion coefficient in the steel and t is the elapsed time (total duration of the notched tensile test), can then be used to calculate the effective diffusion distance for hydrogen diffusion in each particular test.

$$x_H = \sqrt{D_{app} \cdot t} \quad (9)$$

The total duration of the notched tensile tests was given in Table 6, and the apparent diffusion coefficients of the two steels were shown in Table 4. Table 7 now shows these calculated effective hydrogen diffusion distances. As the diffusion distance increases (when tests are performed using lower displacement rates, the time available for hydrogen to reach the notch tip region increases), more and more hydrogen accumulates in the process zone ahead of the notch root and the aforementioned embrittlement micromechanisms develop once a critical hydrogen concentration is reached in this region submitted to high normal stresses.

Displacement rate [mm/min]	Diffusion distance [mm]	
	Fine grain steel (42CrMo4_845-700)	Coarse grain steel (42CrMo4_1200-700)
0.4	0.8	0.35
0.04	1.4	1.2
0.004	4.6	3.4
0.002	7.5	4.8

Table 7. Available effective hydrogen diffusion distance (in mm) in the hydrogen pre-charged notched tensile tests

Fig. 20 shows the embrittlement index related to the reduction in area determined for both steels versus the effective hydrogen diffusion distance, along with the most important embrittlement mechanisms observed in each case.

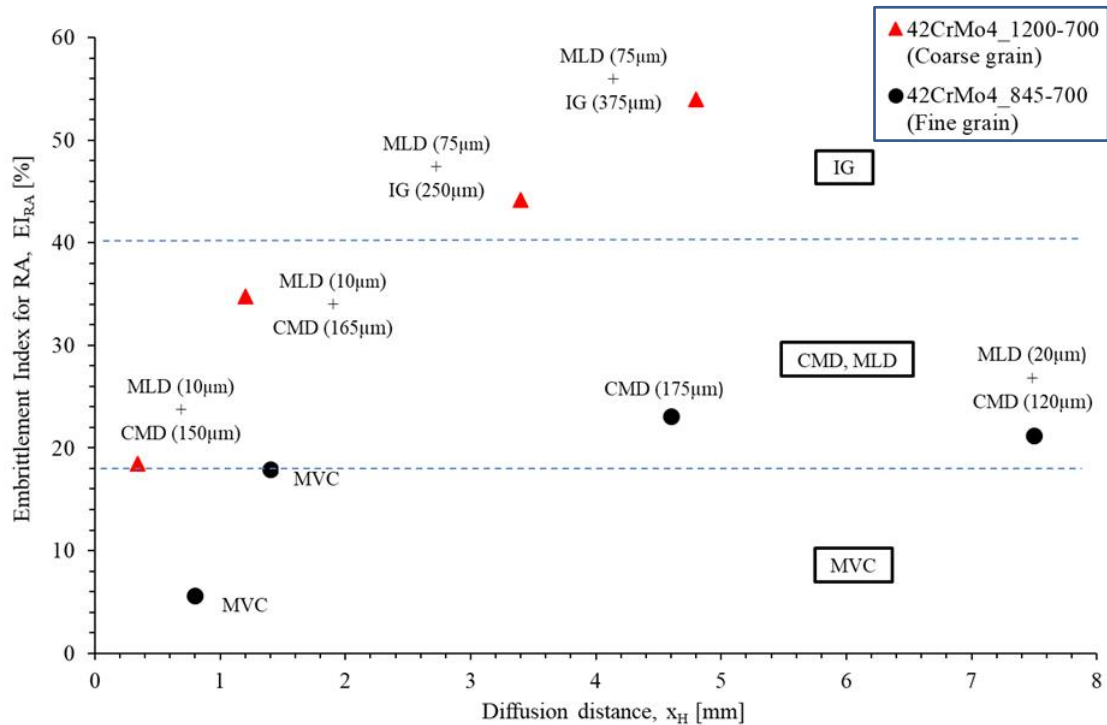


Fig. 20. Embrittlement indexes associated with the reduction in area (RA) versus the effective hydrogen diffusion distance (x_H). Operative fracture micromechanisms in the peripheral region. Hydrogen pre-charged notched tensile specimens

The magnitude of the embrittlement index can now be related to the operative failure micromechanism in this 42CrMo4 steel. For embrittlement indexes lower than 18%, only the HELP mechanism operates, and failure takes place via microvoid coalescence (MVC), where only the presence of very enlarged voids evidences the presence of internal hydrogen. In the case of embrittlement indexes between 18% and around 40%, HEDE mechanisms already take place, namely carbide-matrix interface decohesion (CMD) and martensite lath interface decohesion (LMD). Finally, intergranular fracture (IG) was only observed when the embrittlement index was greater than 40%. It should be borne in mind that, as the effective diffusion distance increases, hydrogen accumulation in the process zone ahead of the notch also increases, giving rise to the modification of the main failure mechanism: from MVC to CMD, MLD and finally IG.

Fig. 20 also shows the effect of the prior austenite grain size on the hydrogen embrittlement of this 42CrMo4 steel. At low diffusion distances, the embrittlement index measured in the fine-grained steel tested under quite large displacement rates, i.e. small diffusion distances, is low (<20%) and a characteristic ductile micromechanism, MVC, was observed. However, under the same testing conditions, MLD and CMD embrittlement mechanisms are already operative in the coarse-grained steel and the corresponding embrittlement indexes increase. These same micromechanisms operate in the fine-grained steel under large effective diffusion distances, giving rise to slightly higher embrittlement indexes. Under the same testing conditions, however, the most important failure mechanism in the case of the coarse-grained steel was intergranular failure (IG) and the embrittlement index significantly increases ($EI > 40\%$).

5. CONCLUSIONS

The higher thermal drop produced when the 42CrMo4 steel grade is quenched from 1200°C (coarse-grained microstructure formed in the CG-HAZ of its welds) instead of 845°C (fine-grained steel produced in a conventional Q+T treatment) gives rise to a more distorted martensitic structure, with higher internal stresses and hence higher dislocation density, thus explaining the larger deeply trapped hydrogen capability of this coarse-grained microstructure. A similar explanation also justifies the slightly lower value of the hydrogen diffusion coefficient calculated with the coarse-grained steel ($2.51 \times 10^{-10} \text{ m}^2/\text{s}$) compared to the fine-grained base steel ($4.34 \times 10^{-10} \text{ m}^2/\text{s}$).

In the absence of hydrogen, the steel with the largest prior austenitic grain size exhibits higher strength, accompanied by its greater hardness, while the ductility parameters were approximately similar in both steel grades.

Minor differences were detected between tensile tests carried out on smooth uncharged and hydrogen pre-charged specimens of both steels, regardless of the applied displacement rate. No significant change in the failure micromechanism was observed in these tests, microvoid coalescence (MVC) being the only failure micromechanism detected in the entire fracture surface of all these specimens.

On the other hand, only a slight decrease in the tensile notched strength was appreciated in both steel grades for displacement rates lower than 0.4 mm/min (the embrittlement indexes remained almost constant and always below 10%), while properties related to ductility were those most affected by hydrogen, especially in the tests performed under the lowest displacement rates. The embrittlement index related to the reduction in area, $EI_{(RA)}$, reached values of over 20% and 50%, respectively, for the finer- and coarser-grained steels when tested under the lowest displacement rate. Hydrogen embrittlement micromechanisms were observed in these tests (carbide-matrix interface decohesion, CMD and martensite lath interface decohesion, MLD), which extended into the region submitted to maximum hydrostatic stress ahead of the notch tip. Intergranular fracture, IG, was also observed in the case of the coarse-grained steel under the most demanding conditions (lowest displacement rates). The available effective hydrogen diffusion distance for the movement of hydrogen atoms during the notched tensile tests was used to justify the extension of the hydrogen embrittlement micromechanisms.

AKNOWLEDGEMENTS

The authors would like to thank the Spanish Ministry of Science, Innovation and Universities for the financial support received to carry out research project RTI2018-096070-B-C31 (H2steelweld), and A. Zafra to the Ministry of Education and Culture of the Principality of Asturias for the Severo Ochoa grant (PA-18-PF-BP17-038). Authors also thank the financial support received from the Principado de Asturias government through the FC-GRUPIN-IDI/2018/000134 project.

REFERENCES

- [1] R. Von Helmolt, U. Ebele, Fuel cell vehicles: status 2007. *J. Power Sources* 165 (2007) 833-43.
- [2] R.P. Gangloff, B.P. Somerday, Edit. Gaseous hydrogen embrittlement of materials in energy technologies, Woodhead Publishing Limited, 2012
- [3] K. Takasawa, R. Ikeda, N. Ishikawa, R. Ishigaki, Effects of grain size and dislocation density on the susceptibility to high-pressure hydrogen environment embrittlement of high-strength low-alloy steels, *Int. J. of Hydrogen Energy* 37 (2012) 2669-2675.

- [4] A. Zafra, L.B. Peral, J. Belzunce, C. Rodríguez, Effects of hydrogen on the fracture toughness of CrMo and CrMoV steels quenched and tempered at different temperatures, *Int. J. of Hydrogen Energy* 44 (2019) 3953-3965.
- [5] A. Macadre, M. Artamonov, S. Matsuoka, J. Furtado, Effects of hydrogen pressure and test frequency on fatigue crack growth properties of Ni-Cr-Mo steel candidate for storage cylinder of a 70 MPa hydrogen filling station, *Eng. Fract. Mech.* 78 (2011) 3196-3211.
- [6] S. Matsuoka, H. Tanaka, N. Homma, Y. Murakami, Influence of hydrogen and frequency on fatigue crack growth behaviour of Cr-Mo steel, *Int. J. of Fracture* 168 (2011) 101-112.
- [7] C. Colombo, G. Fumagalli, F. Bolzoni, G. Gobbi, L. Vergani, Fatigue behaviour of hydrogen pre-charged low alloy Cr-Mo steel, *Int. J. of Fatigue* 83 (2016) 2-9.
- [8] J. Yamabe, T. Awane, S. Matsuoka, Investigation of hydrogen transport behaviour of various low-alloy steels with high-pressure hydrogen gas, *Int. J. of Hydrogen Energy* 40 (2015) 11075-11080.
- [9] Z. Hua, X. Zhang, J. Zheng, C. Gu, T. Cui, Y. Zhao, W. Peng, Hydrogen-enhanced fatigue life analysis of Cr-Mo Steel high pressure vessels, *Int. J. of Hydrogen Energy* 42 (2017) 12005-12014.
- [10] N. de Miguel, B. Acosta, P. Moretto, L. Briottet, P. Bortot, E. Mecozzi, Hydrogen enhanced fatigue in full scale metallic vessel tests. Results from the MATHYRCE project, *Int. J. of Hydrogen Energy* 42 (2017) 13777-13788.
- [11] T. Zhang, W. Zhao, Q. Deng, W. Jiang, Y. Wang, Y. Wang, W. Jiang, Effect of microstructure inhomogeneity on hydrogen embrittlement susceptibility of X-80 welding HAZ under pressurized gaseous hydrogen, *Int. J. of Hydrogen Energy* 42 (2017) 25102-25113.
- [12] V. Olden, A. Alvaro, O.M. Akselsen, Hydrogen diffusion and hydrogen influenced critical stress intensity in an API X-70 pipeline steel welded joint – Experiments and FE simulations, *Int. J. of Hydrogen Energy* 37 (2012) 11474-86.
- [13] J.J.A. Wang, F. Ren, T. Tan, K. Liu, The development of in situ fracture toughness evaluation techniques in hydrogen environment, *Int. J. of Hydrogen Energy* 40 (2015) 2013-24.
- [14] S. Pillot, L. Coudreuse, Hydrogen-induced disbonding and embrittlement of steels used in petrochemical refining, Woodhead Publishing Limited, 2012.
- [15] P.A.S. Pereira, C.S.G. Franco, J.L.M. Guerra Filho, D.S. dos Santos, Hydrogen effects on the microstructure of a 2.25Cr-1Mo-0.25V steel welded joint, *Int. J. of Hydrogen Energy* 40 (2015) 17136-17143.
- [16] A. Alvaro, V. Olden, A. Macadre, O.M. Akselsen, Hydrogen embrittlement susceptibility of a weld simulated X70 heat affected zone under H₂ pressure, *Mat. Sci. and Eng. A* 597 (2014) 29-36.
- [17] L.R.O. Costa, L.F. Lemus, D.S. dos Santos, Hydrogen embrittlement susceptibility of welded 2.25Cr-1Mo Steel under elastic stress, *Int. J. of Hydrogen Energy* 40 (2015) 17128-17135.
- [18] Q. Wang, Y. Sun, S. Gu, Z. He, Q. Wang, F. Zhang, Effect of quenching temperature on sulfide stress cracking behavior of martensitic steels, *Mat. Sci. & Eng. A* 724 (2018) 131-141.
- [19] L.W. Tsay, C.C. Liu, Y.H. Chao, Y.H. Shieh, Fatigue crack propagation in 2.25Cr1Mo steel weldments in air and hydrogen, *Mat. Sci. and Eng. A* 299 (2001) 16-26.
- [20] C. San Marchi, B.P. Somerday, Sandia Report, SAND2008-1163, 2008.

- [21] S. P. Lynch, Hydrogen embrittlement (HE) phenomena and mechanisms, Chapter 2 in Stress corrosion cracking: theory and practice, V.S. Raja and T. Shoji (Edit.), Woodhead Publishing Ltd., 2011
- [22] A.R. Troiano, The role of hydrogen and other interstitials in the mechanical behavior of metals, *Trasn. ASM* 52 (1960) 54-80.
- [23] R.A. Oriani, A mechanistic theory of hydrogen embrittlement of steels, *Ber. Bunsenges. Phys. Chem.* 76 (1972) 848-857.
- [24] H.K. Birnbaum, Mechanisms of hydrogen related fracture of metals, pp 639-658, in *Hydrogen Effects on Materials Behaviour*, N.R. Moody and A.W. Thompson (Edit.), TMS, Warrendale, PA, 1990
- [25] H.K. Birnbaum, P. Sofronis, Hydrogen-enhanced localized plasticity- a mechanism for hydrogen-related fracture, *Mater. Sci. Eng. A* 176 (1994) 191-202.
- [26] H.K. Birnbaum, I.M. Robertson, P. Sofronis, Hydrogen effects on plasticity, pp 367-381, in *Multiscale Phenomena in Plasticity*, J. Lepinoux et al. (Edit.), Kluwer Academic, Norwell, MA, 2000.
- [27] A. Zafra, L.B. Peral, J. Belzunce, C. Rodríguez, Effect of hydrogen on the tensile properties of 42CrMo4 steel quenched and tempered at different temperatures, *Int. J. of Hydrogen Energy* 43 (2018) 9068-9082.
- [28] A.Zafra, L.B. Peral, J. Belzunce, C. Rodríguez, Effects of hydrogen on the fracture toughness of 42CrMo4 steel quenched and tempered at different temperatures, *Int. J. Pressure Vessels and Piping* 171 (2019) 34-50.
- [29] L.B. Peral, A. Zafra, S. Blasón, C. Rodríguez, J. Belzunce, Effect of hydrogen on the fatigue crack growth rate of quenched and tempered CrMo and CrMoV steels, *Int. J. of Fatigue* 120 (2019) 201-214.
- [30] G.E. Linnert, *Welding Metallurgy*, vol. 1, American Welding Society, Miami, Florida, USA, 1994.
- [31] *Thermal properties of metals*, Edit. F. Cverna, ASM International, Materials Park, Ohio, USA, 2002.
- [32] C.R. Brooks, *Principles of the heat treatment of plain carbon and low alloyed steels*, ASM International, Materials Park, Ohio, USA, 1996
- [33] ASTM G146, "Evaluation of disbonding of bimetallic stainless alloy/steel plate for use in high-pressure, high temperature refinery hydrogen service", *Annual Book of ASTM Standards*, Vol. 03.02, 2013.
- [34] J.P. Hirtz, Effects of hydrogen on the properties of iron and steel, *Metall. Trans. A.* 11 (1980) 861-890.
- [35] C. San Marchi, B.P. Somerday, S.L. Robinson, Permeability, solubility and diffusivity of hydrogen isotopes in stainless steels at high gas pressures, *Int. J. of Hydrogen Energy* 32 (2007) 100-116.
- [36] F.D. Fisher, G. Mori, J. Svoboda, Modelling the influence of trapping on hydrogen permeation in metals, *Corr. Sci.* 76 (2013) 382-389.
- [37] ISO 6892-1:2017. *Metallic materials. Tensile testing - Part 1: Method of test at room temperature.*
- [38] H. Neuber, F. A. Raven, and J. S. Brock, *Theory of Notch Stresses: principles for exact stress calculation.* Berlin: Julius Springer, 1937.
- [39] M. Wang, E. Akiyama, and K. Tsuzaki, Effect of hydrogen on the fracture behavior of high strength

steel during slow strain rate test, *Corros. Sci.* 49, 11 (2007) 4081–4097.

- [40] S. Takagi, S. Terasaki, K. Tsuzaki, T. Inoue, and F. Minami, Application of Local Approach to Hydrogen Embrittlement Fracture Evaluation of High Strength Steels, *Mat. Sci. Forum* 539-543, (2007) 2155–2161.
- [41] N. Parvathavarthini, S. Saroja, R.K. Dayal, H.S. Khatak, Studies on hydrogen permeability of 2.25Cr-1Mo ferritic steel: correlation with microstructure, *J. of Nuclear Mat.* 288 (2001) 187-196.
- [42] K. Takasawa, R. Ishigaki, Y. Wada, R. Kayano, Absorption of hydrogen in high-strength low-alloy steel during tensile deformation in gaseous hydrogen, *ISIJ International* 50, 10 (2010) 1496-1502.
- [43] H.K.D.H. Badeshia. Prevention of hydrogen embrittlement in steels, *ISIJ International* 56, 1 (2016) 24-36.
- [44] J.Y.Lee and J.L. Lee, A trapping theory of hydrogen in pure iron. *Philos. Mag. A* 57, 3 (1987) 293-309.
- [45] A. Nagao, K. Hayashi, K. Oi, S. Mitao, Effect of uniform distribution of fine cementite on hydrogen embrittlement of low carbon martensitic steel plates, *ISIJ International* 52, 2 (2012) 213-221.
- [46] D. Li, R.P. Gangloff, J.R. Scully, Hydrogen trap states in ultrahigh-strength AERMET 100 steel, *Metall. and Mater. Trans. A* 35, 3 (2004) 849-864.
- [47] George Krauss, *Steels: Processing, Structure and Performance*. 2005.
- [48] M. Wang, E. Akiyama, K. Tsuzaki, Effect of hydrogen and stress concentration on the notch tensile strength of AISI 4135 steel, *Mater. Sci. Eng. A* 398 (2005) 37-46.
- [49] K. A. Nibur, B. P. Somerday, C. S. A. N. Marchi, J. W. Foulk, M. Dadfarnia, and P. Sofronis, The Relationship Between Crack-Tip Strain and Subcritical Cracking Thresholds for Steels in High-Pressure Hydrogen Gas, *Metall. Mater. Trans. A* 44 (2013) 248–269.
- [50] I. M. Robertson, P. Sofronis, A. Nagao, M.L. Martins, S. Wang, D.W. Gross and K.E. Nygren, Hydrogen embrittlement understood, *Metall. Mat. Trans. A* 46, 6 (2015) 2323-2341.
- [51] A. Nagao, M. Dadfarnia, B.P. Somerday, P. Sofronis, R.O. Ritchie, Hydrogen-enhanced-plasticity mediated decohesion for hydrogen-induced intergranular and quasi-cleavage fracture of lath martensitic steels, *J. Mech. Phys. Solids* 112 (2018) 403-430.